

Journal of Geophysical Research: Space Physics

RESEARCH ARTICLE

10.1002/2015JA021792

Key Points:

- Callisto's atmosphere/ionosphere is important in the Moon's interaction with Jupiter's magnetosphere
- Magnetic signals driven by the magnetosphere-ionosphere interaction can obscure induction signals
- Callisto's pickup tail is flat and asymmetric, driven by large gyroradii of ionospheric pickup ions

Correspondence to:

L. Liuzzo,
lucas.liuzzo@eas.gatech.edu

Citation:

Liuzzo, L., M. Feyerabend, S. Simon, and U. Motschmann (2015), The impact of Callisto's atmosphere on its plasma interaction with the Jovian magnetosphere, *J. Geophys. Res. Space Physics*, 120, 9401–9427, doi:10.1002/2015JA021792.

Received 12 AUG 2015

Accepted 21 OCT 2015

Accepted article online 22 OCT 2015

Published online 12 NOV 2015

The impact of Callisto's atmosphere on its plasma interaction with the Jovian magnetosphere

Lucas Liuzzo¹, Moritz Feyerabend^{1,2}, Sven Simon¹, and Uwe Motschmann^{3,4}

¹School of Earth and Atmospheric Sciences, Georgia Institute of Technology, Atlanta, Georgia, USA, ²Institute of Geophysics and Meteorology, University of Cologne, Cologne, Germany, ³Institute for Theoretical Physics, University of Braunschweig, Braunschweig, Germany, ⁴Institute for Planetary Research, German Aerospace Center, Berlin, Germany

Abstract The interaction between Callisto's atmosphere and ionosphere with the surrounding magnetospheric environment is analyzed by applying a hybrid simulation code, in which the ions are treated as particles and the electrons are treated as a fluid. Callisto is unique among the Galilean satellites in its interaction with the ambient magnetospheric plasma as the gyroradii of the impinging plasma and pickup ions are large compared to the size of the moon. A kinetic representation of the ions is therefore mandatory to adequately describe the resulting asymmetries in the electromagnetic fields and the deflection of the plasma flow near Callisto. Multiple model runs are performed at various distances of the moon to the center of Jupiter's magnetospheric current sheet, with differing angles between the corotational plasma flow and the ionizing solar radiation. When Callisto is embedded in the Jovian current sheet, magnetic perturbations due to the plasma interaction are more than twice the strength of the background field and may therefore obscure any magnetic signal generated via induction in a subsurface ocean. The magnetic field perturbations generated by Callisto's ionospheric interaction are very similar at different orbital positions of the moon, demonstrating that local time is only of minor importance when disentangling magnetic signals generated by the magnetosphere-ionosphere interaction from those driven by induction. Our simulations also suggest that deflection of the magnetospheric plasma around the moon cannot alone explain the density enhancement of 2 orders of magnitude measured in Callisto's wake during Galileo flybys. However, through inclusion of an ionosphere surrounding Callisto, modeled densities in the wake are consistent with in situ measurements.

1. Introduction

Jupiter's second largest moon Callisto (radius $R_C = 2410$ km) orbits its parent planet at a distance of $26.3 R_J$ (radius of Jupiter $R_J = 71492$ km) and with an orbital period of 16.7 days. Featuring an inclination of only 0.19° , Callisto's orbit is located within Jupiter's rotational equatorial plane. However, since Jupiter's magnetic moment is tilted by 9.6° with respect to the planet's rotation axis, Jupiter's magnetospheric magnetic field and associated current sheet exhibit strong oscillatory variations at the orbital position of Callisto [Khurana, 1997]. The timescale of these oscillations is mainly defined by the planet's synodic rotation period of 10.18 h [e.g., Neubauer, 1998; Seufert et al., 2011]. Additional variability in the ambient magnetospheric field conditions may arise from, for example, contributions of Jupiter's magnetopause currents near Callisto.

During 7 Galileo spacecraft flybys of Callisto between 1996 and 2001, the onboard magnetometer instrument collected data in the immediate vicinity of the moon (see Table 1 for the naming of the flybys). Data from two of these flybys (C3 and C9) showed a local dipolar field structure at Callisto superimposed on the background Jovian magnetospheric field. Several studies have ascribed these perturbations to the presence of an electrically conducting water ocean beneath the surface of the moon, which generates magnetic signatures outside of the moon via electromagnetic induction [Khurana et al., 1998; Kivelson et al., 1999; Zimmer et al., 2000]. By assuming that the magnetic perturbations were generated exclusively by currents induced in Callisto's interior, Zimmer et al. [2000] found magnetic field flyby data from C3 and C9 to be consistent with an ocean at a depth of approximately 170 km.

The magnetopause of Jupiter is located at a standoff distance between approximately 45 and $100 R_J$ depending on ambient solar wind conditions [Joy et al., 2002]. Therefore, Callisto interacts with the Jovian magnetospheric plasma environment and is never exposed to the solar wind. Callisto's orbital period is much larger

Table 1. Galileo Spacecraft Flybys of Callisto With Their Abbreviations and Dates^a

Flyby	Date	α_{\odot} (deg)	LT (h)	h_{cs} (R_J)	C/A (km)	MAG	Io	PI
C3	4 Nov 1996	116.8	07:47	3.24	1135.9	×	×	×
C9	25 Jun 1997	83.0	05:32	-3.52	418.1	×	×	×
C10	17 Sep 1997	75.5	05:02	-2.45	535.3	×	×	×
C20	5 May 1999	267.5	17:50	2.93	1321.4		×	
C21	30 Jun 1999	26.1	01:44	-1.87	1048.1	×	×	×
C22	14 Aug 1999	272.0	18:08	-4.31	2299.3	×	×	×
C23	16 Sep 1999	268.8	17:55	1.08	1052.4	×	×	×
C30	25 May 2001	197.5	13:10	3.50	131.9	×	×	×

^aThe symbol α_{\odot} is the solar phase angle of Callisto during the flyby, and LT is the corresponding local time. Represented by h_{cs} is the distance of Callisto above ($h_{cs} > 0$) or below ($h_{cs} < 0$) the center of the Jovian current sheet [Bagenal and Delamere, 2011], with C/A the closest approach altitude of Galileo. The cross indicates the flybys for which data from the magnetometer (MAG), ionospheric occultation technique (Io), or the plasma instrument (PI) are available. This table has been adopted from Seufert [2012].

than Jupiter's rotation period, so plasma approximately corotating with Jupiter continuously overtakes the moon at a relative velocity of about 192 km/s [Kivelson et al., 2004]. Callisto therefore represents an obstacle to the incident magnetospheric plasma flow, and this interaction imposes additional perturbations on the electromagnetic fields and plasma flow pattern near the moon.

Unlike Jupiter's largest satellite Ganymede, Callisto was found to be devoid of an internally generated dynamo field [Khurana et al., 1997; Zimmer et al., 2000]. This implies that impinging magnetospheric plasma may interact with Callisto's atmosphere and ionosphere in addition to an induced magnetic field at the moon. This atmosphere primarily arises from sputtering of the surface materials by energetic magnetospheric particles [Kliore et al., 2002; Liang et al., 2005; Vorburger et al., 2015]. The Galileo spacecraft's Near-Infrared Mapping Spectrometer measured the presence of a CO₂ atmosphere around Callisto with a surface density of $4 \cdot 10^8 \text{ cm}^{-3}$ and a scale height of 23 km [Carlson, 1999]. In using a Monte Carlo approach to model the neutral components of Callisto's atmosphere, Vorburger et al. [2015] suggest that this CO₂ may arise from a combination of sputtering as well as sublimation of surface ices.

Independent evidence for the existence of an atmosphere around Callisto was found in radio occultation measurements of ionospheric electron densities by Kliore et al. [2002]. However, the remarkably high peak electron densities of $15,300 \text{ cm}^{-3}$ and $17,400 \text{ cm}^{-3}$ detected during Galileo's C22 and C23 flybys of Callisto cannot arise from solar ultraviolet and electron impact ionization of the CO₂ atmospheric component alone. To resolve this discrepancy, Kliore et al. [2002] postulated the existence of an additional O₂ atmospheric component with a column density of $N_{O_2} = 3 \cdot 10^{16} \text{ cm}^{-2}$. Liang et al. [2005] made use of ionization of a one-dimensional atmosphere model to confirm the density result from Kliore et al. [2002] and obtained an O₂ column density value of $N_{O_2} = 9.6 \cdot 10^{16} \text{ cm}^{-2}$. Recently, Cunningham et al. [2015] have further corroborated the existence of an O₂ atmosphere at Callisto with the Hubble Space Telescope. From measurements of O atomic line spectra in Callisto's atmosphere, they were able to infer an O₂ column density of $N_{O_2} = 4 \cdot 10^{15} \text{ cm}^{-2}$ located in the sub-Jovian hemisphere of Callisto (i.e., the hemisphere facing Jupiter). However, this value is an order of magnitude lower than the values suggested by Kliore et al. [2002] and Liang et al. [2005].

Callisto's neutral atmosphere is ionized by three processes: photoionization, electron impact ionization, and charge exchange collisions with incident magnetospheric plasma. Once ionized, the charged particles are picked up by the ambient electromagnetic fields thereby draining momentum from the incident magnetospheric plasma flow and disturbing both the flow pattern and the electromagnetic fields near the moon. Since Callisto's position with respect to Jupiter's equatorial current sheet strongly varies during the course of one planetary rotation [Khurana, 1997; Kivelson et al., 2004], a broad variety of different plasma interaction scenarios with the ionosphere occur at Callisto. On the one hand, when Callisto is embedded in Jupiter's magnetospheric current sheet, the moon may be exposed to a super-Alfvénic yet subsonic and submagnetosonic plasma flow, with the gyroradii of magnetospheric and ionospheric particles on the order of $10 R_C$ (see Table 2). For these upstream conditions, Callisto's plasma interaction is highly similar to the interaction between Saturn's largest moon, Titan, and its parent planet's magnetosphere [Neubauer et al., 1984, 2006].

Table 2. Plasma Simulation Parameters Used for the Model Runs^a

Parameter	Symbol	Current Sheet	Magnetodisk Lobe
Background magnetic field (nT)	\mathbf{B}_0	4	40
Upstream magnetospheric ion velocity (km/s)	\mathbf{u}_0	192	192
Upstream magnetospheric ion thermal velocity (km/s)	v_{th}	212	212
Upstream magnetospheric ion number density (cm^{-3})	n_0	0.1	0.1
Upstream magnetospheric ion mass (amu)	m_0	16	16
Ion plasma beta	β_i	10	0.1
Electron plasma beta	β_e	0.13	0.0013
Alfvénic Mach number	M_A	2.77	0.277
Magnetosonic Mach number	M_{MS}	0.835	0.270
O ⁺ magnetospheric ion gyroradius (R_C)	r_{g,O^+}	3.31	0.331
CO ₂ ⁺ pickup ion gyroradius (R_C)	r_{g,CO_2^+}	9.08	0.908
O ₂ ⁺ pickup ion gyroradius (R_C)	r_{g,O_2^+}	6.61	0.661

^aValues correspond to either a Jovian current sheet or Jovian magnetodisk lobe configuration and are adapted from Kivelson *et al.* [2004] and Belcher [1983].

On the other hand, when Callisto is located in one of Jupiter's magnetodisk lobes, the moon may interact with a sub-Alfvénic and submagnetosonic plasma flow. Even in this scenario, the gyroradii of atmospheric pickup ions are still comparable to the radius of the moon (Table 2). The transverse currents generated in Callisto's ionosphere are then closed by a current system flowing along the characteristics of an Alfvén wing, i.e., a system of nonlinear standing Alfvén waves that connect the moon to Jupiter's polar ionosphere [Neubauer, 1980, 1998]. Similar sub-Alfvénic interaction scenarios also occur at the three remaining Galilean moons [e.g., Saur *et al.*, 1999] and the Saturnian moon Enceladus [e.g., Dougherty *et al.*, 2006].

As described above, initial studies of Callisto's magnetic environment considered only the induced, dipolar magnetic fields generated via currents in the moon's putative subsurface ocean and have mainly focused on the C3 and C9 flybys that occurred when the moon was located far above or below the Jovian current sheet (Table 1). For those scenarios, the magnetic fields generated by the plasma interaction were weak compared to those generated by induction [Zimmer *et al.*, 2000]. However, when Callisto is located near the center of the Jovian magnetospheric current sheet, the magnetosphere-ionosphere interaction may make a nonnegligible contribution to the magnetic perturbations near Callisto. For a schematic of which process is expected to dominate for each of the seven flybys with magnetometer data available, see Figure 1a. When embedded in the Jovian current sheet ($h_{cs} = 0$ in the figure), the perturbations of the magnetic field are generated mainly by currents in the ambient plasma, whereas the magnetic signal generated by induction minimizes. Far from the current sheet ($h_{cs} < 0$ or $h_{cs} > 0$ in the figure), plasma currents are minimal and the dominant magnetic field signature is a result of currents induced in the subsurface ocean.

In addition to the C3 and C9 flybys, Kivelson *et al.* [1999] studied the C10 flyby with a purely electromagnetic induction technique but found that the currents outside of the moon driven by the plasma interaction generated magnetic perturbations that were too large to ignore. As visible in Figure 1a, many of the remaining flybys occur at locations where the plasma interaction and induction should both contribute in a nonnegligible way to the perturbations of the ambient magnetic field. For these flybys, a complex scenario occurs at Callisto. Assuming a radially symmetric conductance profile in the interior of the moon and a spatially homogeneous background magnetic field, the time-varying Jovian magnetic field drives currents in the interior of the moon which manifest as an induced magnetic dipole field outside of Callisto [Zimmer *et al.*, 2000]. The induced dipole poses an obstacle to the impinging plasma flow which is deflected around the moon. Because the inducing field near Callisto is then perturbed by the deflection of plasma, the amount of induction that can occur in the interior of the moon is directly affected. In addition to flow deviation caused by an induced dipole, the magnetospheric plasma is decelerated and deflected through mass loading from Callisto's ionosphere. Additionally, a coupling between the magnetosphere-dipole and magnetosphere-ionosphere interactions occurs, as the induced dipole may partially prevent the ambient magnetospheric plasma from impinging

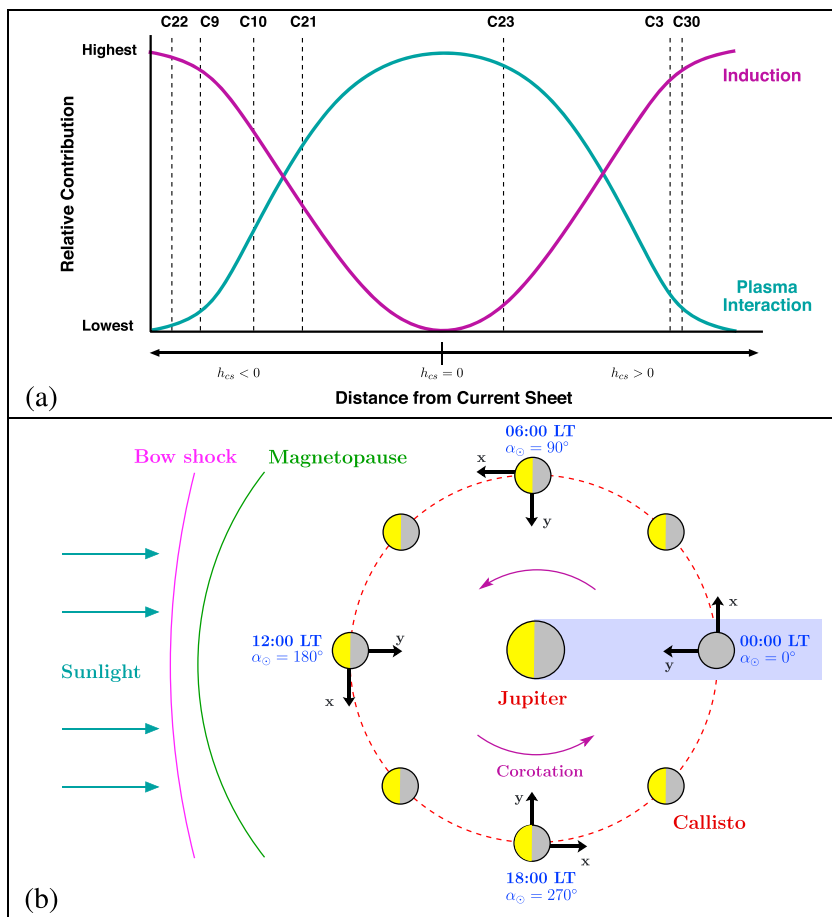


Figure 1. (a) Schematic of the relative contributions of magnetic field perturbations driven by plasma currents (cyan) due to the magnetospheric plasma interaction with Callisto's ionosphere and a dipole and induced currents (purple) in a subsurface ocean that occur at Callisto for each flyby. As the moon's position with respect to the Jovian current sheet changes during each orbit (denoted as h_{CS} , with positive or negative values of h_{CS} corresponding to the moon above or below the current sheet), the method driving magnetic perturbations near Callisto changes until either ambient plasma currents or induced subsurface currents dominate the magnetic signal. (b) The orbital configuration of Callisto around Jupiter for various local times (LT) and corresponding solar phase angles (α_{\odot}). The violet arrows represent the direction of magnetospheric plasma flow as it corotates with Jupiter and overtakes the moon. Superimposed beneath the moon are the x and y axes of the Callisto-centered CphiO coordinate system, in which x aligns with plasma corotation, y points toward Jupiter, and z (i.e., the axis out of the plane of the figure) aligns with the Jovian spin axis. Also represented are incoming solar radiation in cyan, the location of Jupiter's bow shock with an average distance of $\sim 84 R_J$ in magenta and the location of the Jovian magnetopause with an average standoff distance of $\sim 70 R_J$ in green. As Callisto orbits Jupiter at a distance of $26.3 R_J$, at only one location (18:00 LT) does the incident plasma flow aligns with the direction of the ionizing solar ultraviolet radiation. For the other orbital positions, the ramside and dayside hemispheres of the moon are not colocated. The figure is not to scale.

on the ionosphere of Callisto. Thus, a complex mutual interplay between induction, magnetosphere-dipole interaction, and magnetosphere-ionosphere interaction exists at Callisto. A fully self-consistent model of Callisto's magnetic environment must therefore account for the high level of interconnection of these processes [Neubauer, 1999].

Khurana et al. [1998], Kivelson et al. [1999], and Zimmer et al. [2000] were the first to consider electromagnetic induction at Callisto in isolation, one of the three key components to the complex scenario described above. Recently, *Lindkvist et al. [2015]* studied a second component of the interaction in isolation. These authors analyzed the Jovian magnetospheric plasma near the moon as it impinges on a constant induced dipole with a hybrid plasma model (kinetic ions and fluid electrons). The authors were able to confirm the results from *Zimmer et al. [2000]*, who stated that the magnetic signatures measured during C3 and C9 were almost completely associated with an induced magnetic dipole. *Lindkvist et al. [2015]* also showed that the

magnetospheric plasma interaction with the induced dipole alone is not sufficient to reproduce the magnetic field perturbations observed during the C10 flyby. This suggests that an ionosphere surrounding the moon is required to accurately model magnetic field data obtained near Callisto.

However, no such study exists to investigate the interaction of the Jovian magnetospheric environment with the atmosphere and ionosphere of Callisto. This void is filled by the present study. In modeling the magnetosphere-ionosphere interaction of Callisto in isolation, this paper is complementary to previous studies in the attempt to understand each individual component of the entangled Callisto interaction scenario. Considerable evidence exists that the atmosphere surrounding the moon is an important component of the plasma interaction. *Gurnett et al.* [1997, 2000] measured plasma densities 2 orders of magnitude larger than the magnetospheric background density in Callisto's wake during C3 and C10, respectively, and connected these increases to an ionosphere interacting with the impinging magnetospheric plasma. The wakeside plasma density increase modeled by *Lindkvist et al.* [2015] is not large enough to explain these observational data, providing strong evidence that the magnetosphere-ionosphere interaction at Callisto may indeed be as important as the other two components of the entangled scenario described above. Independent evidence for the importance of Callisto's ionosphere to the plasma interaction was presented by *Strobel et al.* [2002]. In using an analytical model to consider only the magnetosphere-ionosphere interaction, these authors demonstrate that an intense coupling of Callisto's ionosphere with the Jovian magnetosphere must occur due to strong transverse ionospheric conductances. *Strobel et al.* [2002] also suggest that the high conductances of Callisto's ionosphere may create magnetic field perturbations of approximately 12 nT, similar to the values that *Zimmer et al.* [2000] attribute to induction in a subsurface ocean alone.

Hence, an understanding of the interaction of magnetospheric plasma with Callisto's atmosphere in isolation from induction in a subsurface ocean and plasma interaction with the induced field is critical to further constrain the conductivity, thickness, and depth of the putative subsurface ocean with magnetic field data. Such an understanding facilitates future studies that include the full interconnection between magnetosphere-dipole interaction, magnetosphere-ionosphere interaction, and induction signals at the moon.

To accomplish this, we first model the plasma environment of Callisto when the moon is located in the Jovian current sheet, corresponding to the weakest induction and strongest plasma effects. This is done at different orbital positions along the moon's orbit around Jupiter, i.e., for varying angles between the directions of incident magnetospheric plasma flow and incoming solar ultraviolet (SUV) radiation. The different orientations that occur are visible in Figure 1b. Because sputtering may cause the atmosphere (and therefore ionosphere) at Callisto to be densest on the ramside of the moon [Seufert, 2012], the position of the ramside hemisphere with respect to the Sun may change the interaction scenario. Thus, by examining the plasma and electromagnetic perturbations at different orbital positions of the moon, we are able to constrain the robustness of these signatures against changes in the ionospheric configuration. This is a necessary step in any study using an ionosphere at Callisto, as so far, no three-dimensional model of the ionosphere exists. Additionally, because Callisto experiences a change in the strength of the Jovian magnetic field by nearly an order of magnitude over a single orbit, a second simulation is performed. This corresponds to when Callisto is located far from the center of the current sheet in one of Jupiter's magnetodisk lobes, which functions to characterize the interaction at different background field strengths.

The study is structured as follows: a description of the hybrid model (kinetic ions and fluid electrons) used is presented in section 2. A discussion of the simulation setup and model parameters is also presented here. Section 3 presents our hybrid modeling results of the plasma interaction of Callisto's ionosphere with the magnetospheric environment of Jupiter. The study is concluded with brief summary of all major findings in section 4. Finally, results from the hybrid simulation are compared to Galileo flyby data in Appendix A. This is used to validate the model against in situ flyby data.

2. Model of Callisto's Plasma Interaction

2.1. Hybrid Simulation Code A.I.K.E.F.

To study the interaction between Callisto's ionosphere and Jupiter's magnetospheric plasma, the adaptive ion-kinetic, electron fluid hybrid model (A.I.K.E.F.) is used [*Müller et al.*, 2011]. A kinetic description of the ions is mandatory when modeling Callisto's plasma interaction as magnetospheric and ionospheric pickup ions

can have gyroradii up to 10 times the radius of Callisto. In the model, ions are represented by macroparticles that have the same charge-to-mass ratio as a real ion. The Newtonian equations of motion are solved for each individual macroparticle:

$$\frac{d\mathbf{x}_i}{dt} = \mathbf{v}_i \quad , \quad (1)$$

$$\frac{d\mathbf{v}_i}{dt} = \frac{q_i}{m_i} [\mathbf{E} + \mathbf{v}_i \times \mathbf{B}] \quad , \quad (2)$$

with \mathbf{x}_i and \mathbf{v}_i representing the position and velocity, respectively, of an individual macroparticle, electro-magnetic field quantities \mathbf{E} and \mathbf{B} , particle charge q_i , and mass m_i . The electrons are treated as a massless, charge-neutralizing fluid, whose dynamics are solved through the use of a modified Navier-Stokes equation:

$$0 = -en_e [\mathbf{E} + \mathbf{u}_e \times \mathbf{B}] - \nabla P_e + n_e \eta \mathbf{j} \quad , \quad (3)$$

where n_e and \mathbf{u}_e represent the number density and bulk velocity of the electron fluid, respectively, with elementary charge e , current \mathbf{j} , and resistivity η . The electron pressure, P_e , is assumed to be adiabatic, such that

$$P_e = P_0 \left(\frac{n_e}{n_{e,0}} \right)^\kappa \quad , \quad (4)$$

where P_0 and $n_{e,0}$ are the electron pressure and number density, respectively, in the undisturbed magnetospheric upstream plasma. Since the presence of the magnetic field reduces the degrees of freedom of electron motion, an adiabatic exponent of $\kappa = 2$ is chosen [Bößwetter *et al.*, 2004; Bagdonat, 2005; Simon *et al.*, 2007]. Via the assumption of quasi-neutrality, the electron density is equal to the sum over the densities of each ion species ($n_e = \sum_i n_i$), where n_i represents the number density of an individual ion species in the simulation, assuming a singly charged ion population at Callisto [Neubauer, 1998; Kivelson *et al.*, 2004].

With the assumption of singly charged ions leading to $q_i = e$, through application of Ampère's law

$$\mathbf{j} = \frac{1}{\mu_0} \nabla \times \mathbf{B} \quad , \quad (5)$$

and the definition of the current

$$\mathbf{j} = -en_e \mathbf{u}_e + e \sum_i n_i \mathbf{u}_i \quad , \quad (6)$$

with ion bulk velocity \mathbf{u}_i , the electric field can be written as

$$\mathbf{E} = -\mathbf{u}_i \times \mathbf{B} + \frac{[\nabla \times \mathbf{B}] \times \mathbf{B}}{en_i \mu_0} - \frac{\nabla P_e}{en_i} + \frac{\eta}{\mu_0} \nabla \times \mathbf{B} \quad . \quad (7)$$

Finally, these equations are closed via Faraday's law which describes the time evolution of the magnetic field:

$$\frac{\partial \mathbf{B}}{\partial t} = -\nabla \times \mathbf{E} \quad . \quad (8)$$

The hybrid simulation code A.I.K.E.F. has been used in multiple studies of moon-magnetosphere interactions throughout the solar system. These include the plasma interactions at Rhea [Roussos *et al.*, 2008; Simon *et al.*, 2012], Enceladus [Kriegel *et al.*, 2009, 2011, 2014], Tethys [Simon *et al.*, 2009], and Titan [Simon *et al.*, 2007; Simon and Motschmann, 2009; Müller *et al.*, 2010; Feyerabend *et al.*, 2015]. Kriegel *et al.* [2014] made improvements to the code through inclusion of a multicomponent chemistry and charge-exchange model at Enceladus, and Feyerabend *et al.* [2015] enhanced the routine used to photoionize the neutral atmosphere of Titan. Both of these studies also used multiple levels of mesh refinement to obtain a high-resolution grid near the surface of the moon. The improved chemistry model, photoionization routine, and mesh refinement technique are all implemented in this study, as explained in section 2.2. The A.I.K.E.F. model is therefore well equipped to study the plasma interaction of Callisto.

2.2. Hybrid Simulation Setup

The Callisto-centered, Cartesian CphiO coordinate system is used throughout this study to describe the plasma interaction of the moon. For this system, the center of the moon is located at the origin, the undisturbed corotational plasma flow is aligned with the $+x$ axis, $+y$ points toward Jupiter, and $+z$ is aligned with the Jovian spin axis (see Figure 1b for a schematic of this system). Throughout the study, unit vectors along the x axis, y axis, and z axis are denoted as \hat{x} , \hat{y} , and \hat{z} .

In the first step of this study, the dependence of the interaction on the orbital position of Callisto is investigated. Figure 1b shows selected orbital positions of the moon. As Callisto orbits Jupiter, the location of the moon's dayside ionosphere changes with respect to the ramside hemisphere. Thus, to gain a representative sampling of the types of interaction scenarios that may occur, the interaction is investigated for three orbital positions of Callisto. The first is at 18:00 local time (LT) which corresponds to a solar phase angle of $\alpha_{\odot} = 270^{\circ}$. At this local time, the incoming photoionization is aligned with the direction of magnetospheric corotation. The second is at 12:00 LT ($\alpha_{\odot} = 180^{\circ}$) where photoionization and corotation are perpendicular. The final position investigated is 06:00 LT ($\alpha_{\odot} = 90^{\circ}$), which corresponds to an antiparallel alignment of the direction of photoionization and corotation.

Note that the case of $\alpha_{\odot} = 0^{\circ}$ (i.e., 00:00 LT) is not investigated in this study. At this position, Callisto is located in the geometric shadow of Jupiter where no photoionization would be present. A dilute ionosphere would still be present around Callisto here, as electron impact ionization still occurs. However, because the atmosphere would become charged by photoionization immediately before entering Jupiter's shadow, it would be necessary to determine the timescales over which the solar ultraviolet-generated portion of the ionosphere would decay compared to the transit time of the moon through Jupiter's shadow of approximately 5 h. Additionally, while in the shadow, Callisto's surface and atmosphere would cool down and some atmospheric constituents would freeze out. In this case, electron impact would be much less effective. However, while this may occur, Vorburger *et al.* [2015] suggest that O₂ may remain in the moon's atmosphere in its gaseous state. Regardless which scenario occurs at Callisto, each would require a real-time simulation that is not attempted here, although future studies may investigate the effect of these occurrences on the plasma interaction.

To study Callisto's plasma interaction at different positions with respect to the Jovian current sheet, we have carried out simulations with two different background magnetic field values. An overview of the simulation parameters used for the two separate scenarios is given in Table 2. In the first scenario, the moon is embedded in the Jovian magnetospheric current sheet where Jupiter's magnetic field is weakest. A value of $|\mathbf{B}_0| = 4$ nT is chosen for this scenario [Kivelson *et al.*, 2004], where \mathbf{B}_0 is antiparallel to the z axis of the CphiO system. When embedded in the Jovian current sheet, the magnetic signal visible outside of the moon generated by induction in a subsurface ocean is weak and therefore neglected. In the second scenario, the moon is located in one of the magnetodisk lobes of Jupiter. For this simulation, the background magnetic field value is set to $|\mathbf{B}_0| = 40$ nT [Neubauer, 1998; Kivelson *et al.*, 2004]. When the moon is located in a lobe of the Jovian magnetodisk, contributions to the magnetic signal from induction in a subsurface ocean are not negligible in the entangled Callisto interaction scenario. However, our simulations do not take into account any possible contributions to the plasma interaction from an induced dipole field at Callisto because we study the magnetosphere-ionosphere plasma interaction in isolation from other effects. Isolating the impact of the ionosphere on Callisto's plasma interaction largely facilitates future studies of the entangled scenario that consider magnetic signatures driven by a combination of Callisto's ionosphere and an induced dipole field.

All flybys of Callisto occurred either above or below the center of the Jovian current sheet (see Table 1), so some amount of magnetic induction in Callisto's putative subsurface ocean should have been present during each flyby (Figure 1a). Because this study considers the magnetosphere-ionosphere interaction of Callisto in isolation and therefore does not include any magnetic field induced in a subsurface ocean, the magnetic field results from this study are not directly comparable to Galileo magnetometer data. However, to assess the ability of our hybrid model to reflect reality, A.I.K.E.F. has been configured to consider the scenario of a pure magnetosphere-dipole interaction during two separate Galileo flybys in the same manner as Zimmer *et al.* [2000] and Lindkvist *et al.* [2015]. The results of this validation study are presented in Appendix A.

In reality, the background field in the Jovian magnetodisk lobes would be mainly aligned with $\pm\hat{y}$. However, to facilitate the comparison with the results of the current sheet scenario, the magnetodisk lobe simulations have $|\mathbf{B}_0|$ aligned along $-\hat{z}$ as well. This simply corresponds to a rotation of the entire plasma interaction region about the x axis by 90° , but the results are both qualitatively and quantitatively identical in all other respects.

For both scenarios, the upstream plasma is assumed to corotate with a velocity of $|\mathbf{u}_0| = 192 \text{ km/s}$ and consist of O^+ [Kivelson *et al.*, 2004]. When the moon is embedded in the Jovian current sheet, a number density value of $n_0 = 0.1 \text{ cm}^{-3}$ is used [Kivelson *et al.*, 2004]. When Callisto is located in a Jovian magnetodisk lobe, Kivelson *et al.* [2004] suggest that the number density of the unperturbed magnetospheric plasma in the vicinity of Callisto can be between 0.01 and 0.5 cm^{-3} . Due to the weak constraints on the upstream plasma environment at Callisto, and because the value of 0.1 cm^{-3} used for the current sheet scenario is well within the range proposed by Kivelson *et al.* [2004], the unperturbed upstream magnetospheric ion density in the lobe-type scenario is held constant at 0.1 cm^{-3} . A major goal of this study is to explore the impact that a change of the Alfvénic Mach number has on the plasma interaction. A change of the Alfvénic Mach number is accomplished through a change of the background magnetic field strength alone, and changing the upstream number density would not produce qualitatively new results that go beyond the conclusions reached in this study. Table 2 provides the entire parameter regime defined by both the current sheet and lobe-type interaction scenarios.

The plasma flow near Callisto is always submagnetosonic; i.e., no shock forms upstream of the moon. However, a factor of 10 increase of the background field (4 nT versus 40 nT) corresponds to a factor of 10 increase in the Alfvén velocity because the density and velocity remain constant. This reduces the Alfvénic Mach number from 2.8 in the current sheet scenario to 0.28 in the lobe scenario. Thus, whereas the incident flow is super-Alfvénic in the current sheet, the flow is sub-Alfvénic in the magnetodisk lobes (Table 2). The increase in the magnetic field corresponds to a decrease in the gyroradii of the ions as well. When embedded in the current sheet, the gyroradii of O_2^+ and CO_2^+ pickup ions (corresponding to the two atmospheric constituents used in this study; see section 2.3) are nearly 10 times the radius of Callisto, but the gyroradii of the pickup ions when the moon is located in a Jovian lobe are approximately $1 R_C$ (see Table 2). Thus, even with the increased magnetic field strength, a hybrid simulation model is necessary to resolve asymmetries in the perturbations of the magnetic field and plasma flow pattern near the moon due to large ion gyroradii as well as differences between the flow behaviors of light and heavy plasma species.

In all simulation runs for the Jovian current sheet (i.e., for those runs with $|\mathbf{B}_0| = 4 \text{ nT}$), a Cartesian grid with a size of $L_x \times L_y \times L_z = 15R_C \times 15R_C \times 15R_C$ is used. The size of the simulation box extends between $-4.5R_C \leq x \leq 10.5R_C$, $-10.5R_C \leq y \leq 4.5R_C$, and $-7.5R_C \leq z \leq 7.5R_C$. To ensure that asymmetries driven by the large gyroradii of pickup ions are well represented within the simulation box, the center of the moon is offset within the box to a location of $(0.3L_x, 0.7L_y, 0.5L_z)$. Two levels of Callisto-centered mesh refinement are used within the simulation domain, where each level doubles the resolution compared to the previous level. In the coarsest level of refinement, a resolution of 452 km ($0.19 R_C$) per cell is achieved, while in the highest level of mesh refinement a resolution of 113 km ($0.05 R_C$) per cell near the surface of Callisto is obtained.

For the simulation with Callisto embedded in a magnetodisk lobe of Jupiter, a box size of $L_x \times L_y \times L_z = 30R_C \times 30R_C \times 30R_C$ is used, with the simulation domain defined between $-9R_C \leq x \leq 21R_C$, $-21R_C \leq y \leq 9R_C$, and $-15R_C \leq z \leq 15R_C$. However, the resolution of each grid cell and thus the maximum resolution obtained in the highest level of refinement are the same as above. That is, the coarsest level of refinement corresponds to a resolution of 452 km per cell, the first level refines 226 km per cell, and the second level has a resolution of 113 km per cell. For the x and y directions, using a simulation domain this large allows us to determine the overall size of the interaction region.

When the moon is located in one of the Jovian magnetodisk lobes, the Alfvén wing emanates from the moon's ionosphere and is inclined against the background field at an angle of $\theta = \arctan(M_A) = 15^\circ$ [Neubauer, 1980]. It is therefore able to reach the top and bottom of the simulation domain and may potentially reflect [e.g., Kriegel, 2014]. The reflected Alfvén waves could then interact with the plasma near the moon and cause perturbations that are not physically accurate to the interaction. One way to avoid these problems is to increase the size of the simulation domain in the z direction as done here for the lobe scenario. As such, the travel-time of an Alfvén wave to the upper or lower face of the simulation domain and back to Callisto is increased compared to the overall simulation runtime. In addition, we apply a similar technique as was used by Kriegel *et al.* [2014] for the plasma interaction near Enceladus: Alfvén waves are damped through the use of layers of increased resistivity near the upper and lower boundaries of the simulation domain.

2.3. Model of Callisto's Atmosphere

The three-dimensional structure of Callisto's atmosphere is unknown, and at the time of this study, no three-dimensional model of the moon's atmosphere was available. Therefore, our modeling study considers

Table 3. Densities of the Atmospheric Constituents of Callisto as Available in the Literature Compared to Those Used in the Asymmetric Atmosphere Model Throughout This Study^a

Author	Constituent	H_s (km)	$n_{s,0}$ (cm^{-3})	N_s (cm^{-2})	ψ (deg)
Carlson [1999]	CO_2	23	$4 \cdot 10^8$	$8 \cdot 10^{14}$	80–90
Strobel <i>et al.</i> [2002]	CO_2	N/A	N/A	$1 \cdot 10^{18}$	N/A
Vorburger <i>et al.</i> [2015]	CO_2	19	$2 \cdot 10^8$	$4 \cdot 10^{14}$	120
Strobel <i>et al.</i> [2002]	O_2	N/A	N/A	$3 \cdot 10^{17}$	N/A
Kliore <i>et al.</i> [2002]	O_2	15–25	$(1\text{--}2) \cdot 10^{10}$	$(3\text{--}4) \cdot 10^{16}$	0
Liang <i>et al.</i> [2005]	O_2	30	$3.2 \cdot 10^{10}$	$9.6 \cdot 10^{16}$	N/A
Cunningham <i>et al.</i> [2015]	O_2	30	$1.3 \cdot 10^9$	$4 \cdot 10^{15}$	90–180
Vorburger <i>et al.</i> [2015]	O_2	N/A	$(5\text{--}7) \cdot 10^9$	$3 \cdot 10^{16}$	120
This study	CO_2	230	$4 \cdot 10^8$	$9.2 \cdot 10^{14}$	160
This study	O_2	230	$1 \cdot 10^{10}$	$2.3 \cdot 10^{16}$	160

^a H_s is the scale height for the atmospheric constituent, $n_{s,0}$ is the surface density, N_s corresponds to the column density, and ψ is the angle between the $-x$ axis and the unit vector from the center of Callisto to the point above the moon's surface where the column density value occurs, as described in the text. N/A represents values that are not available in the respective text.

different representations of Callisto's atmosphere. In the first atmosphere model, by assuming the moon's gravitational acceleration to be constant, an exponential profile for each individual neutral atmospheric species is obtained via the barometric equation

$$n_{s,\text{sym}}(r) = n_{s,0} \exp\left(\frac{R_C - r}{H_s}\right), \quad (9)$$

with $n_{s,0}$ the atmospheric number density at the surface of Callisto, and the total atmospheric density

$$n_{\text{sym}}(r) = \sum_s n_{s,\text{sym}}(r). \quad (10)$$

Here subscript s denotes an individual neutral species, $n_{s,\text{sym}}(r)$ is the number density of that species at a distance $r = \sqrt{x^2 + y^2 + z^2}$ from the center of Callisto, and H_s is the scale height of the neutral species s . The number density of the atmosphere in this first model is dependent only on the distance r to the center of Callisto; i.e., this atmosphere exhibits rotational symmetry. For simplicity, this atmosphere model will be referred to as the "symmetric atmosphere" (denoted by subscript sym in the above equations).

Throughout this study an atmosphere consisting of two neutral species, CO_2 and O_2 , is used. Current estimates for the scale heights of these species range from 15 to 30 km (Table 3). In this study, it is assumed that the two constituents both have the same scale height of 23 km. Although in reality this is not the case ($H_{\text{O}_2} = 1.44 H_{\text{CO}_2}$), the difference in the two scale heights is not resolvable even in regions of highest grid resolution with 113 km resolved per cell. This difference is negligible compared to the overall size of the plasma interaction, as the scale heights are much smaller than the gyroradii of the pickup ions which determine the plasma interaction scales.

In addition, due to limitations in grid resolution associated with the kinetic treatment of ions, it is not feasible to obtain a simulation grid that would suffice to resolve an atmospheric scale height on the order of tens of kilometers. This would entail obtaining a grid resolution of 23 km $\approx 0.01 R_C$ or better while simultaneously resolving Callisto's plasma interaction region with length scales that can be 3 orders of magnitude larger (from Table 2, the gyroradii of the CO_2^+ and O_2^+ pickup ions can be on the order of $10 R_C$). The presence of the large gyroradii, rather than the comparatively small atmospheric scale height, is crucial in determining the asymmetric nature of Callisto's interaction region.

Although multiple levels of mesh refinement are used (section 2.2), it is not possible with current computational capacities to resolve both scales simultaneously. For this reason, the actual scale heights are multiplied by a factor of $H_{\text{rel}} = 10$. This causes a redefinition of equation (9), such that

$$n_{s,\text{sym}}(r) = \frac{n_{s,0}}{H_{\text{rel}}} \exp\left(\frac{R_C - r}{H_s H_{\text{rel}}}\right). \quad (11)$$

Whether using equation (9) or (11), the total column density N_s of the neutral atmosphere, defined as

$$N_s = \int_{r=R_C}^{\infty} n_{s,\text{sym}}(r) dr = n_{s,0} H_s , \quad (12)$$

remains unchanged as the surface density is reduced by a factor of H_{rel} . The same method was used by Seufert [2012] who presented preliminary modeling results of the Callisto interaction using a magnetohydrodynamic simulation code. It is also possible that sputtering of Callisto's surface by magnetospheric ions produces neutral scale heights of this magnitude, thereby providing an a posteriori justification for our approach [Vorburger et al., 2015]. However, even through the use of increased scale heights, the assumption of $H_{O_2} \approx H_{CO_2}$ is still valid. When artificially increasing the atmospheric scale heights by a factor of 10 [Seufert, 2012], the modified scale heights of O₂ and CO₂ would become $H_{O_2} = 331$ km and $H_{CO_2} = 230$ km. Therefore, the difference of $H_{O_2} - H_{CO_2} = 101$ km is still below the resolution threshold of a single cell with 113 km resolution and much smaller than the scales over which the plasma interaction occurs. Moreover, the resolutions used in this study represent the maximum values that have currently been achieved by a hybrid simulation [see also Lindkvist et al., 2015].

Because the net amount of atmosphere in the model is unaffected by the increased scale height, our neutral column density values are directly comparable to those proposed in the literature (cf. Table 3). The increased scale height is still less than 10% the radius of Callisto and approximately 1% the size of the gyroradii of the pickup ions. Furthermore, as shown in Table 1, the closest approach altitude of most Galileo flybys is at least 2 times larger than the increased scale height used in this study. The enhanced scale height will produce only minor quantitative changes to the plasma interaction signatures in the immediate vicinity of the moon which should not be detectable during flybys at altitudes above 500 km (see Table 1). Through this technique, a single scale height of the atmosphere can be resolved within two cells in the simulation.

Although exactly what causes the generation of the neutral atmosphere at Callisto is uncertain, Kliore et al. [2002] propose that sputtering by incident magnetospheric plasma may be the dominant factor. This would cause the hemisphere of highest atmospheric density to be colocated with the ramside hemisphere of the moon [Seufert, 2012]. To address this, we have implemented a second model of the atmosphere. In this representation of the atmosphere, the number density includes an additional dependency on the angle between the $-x$ axis and the unit vector \hat{r} from the center of Callisto to a point (x, y, z) in Callisto's atmosphere. This generates an asymmetry in the number density $n_{s,\text{asym}}$ between the ramside and wakeside hemispheres of the moon. Although the atmosphere still exhibits rotational symmetry about the x axis, because of the asymmetry between the moon's trailing and leading hemispheres, the second atmosphere model will be referred to as the "asymmetric atmosphere" throughout the study. The asymmetric atmosphere is represented as in Seufert [2012] by introducing a factor of $\cos(\frac{\psi}{2})$ into equation (11):

$$n_{s,\text{asym}}(r) = \cos\left(\frac{\psi}{2}\right) \frac{n_{s,0}}{H_{\text{rel}}} \exp\left(\frac{R_C - r}{H_s H_{\text{rel}}}\right) . \quad (13)$$

Here ψ is the angle between the unit vector along the $-x$ axis and the radial unit vector from the center of Callisto to a point (x, y, z) , and subscript asym denotes the asymmetric nature of the atmosphere. The $\cos(\frac{\psi}{2})$ factor creates a line of zero density along $(x > 1R_C, y = 0, z = 0)$ when $\psi = 180^\circ$ and decreases the atmospheric density at every other point compared to the symmetric atmosphere model (except for at the subram point, where $\psi = 0^\circ$).

Using maximum surface densities of $n_{O_2,0} = 1 \cdot 10^{10} \text{ cm}^{-3}$ and $n_{CO_2,0} = 4 \cdot 10^8 \text{ cm}^{-3}$ for O₂ and CO₂ found in the literature, column density values of $N_{O_2} = 2.3 \cdot 10^{16} \text{ cm}^{-2}$ for O₂ and $N_{CO_2} = 9.2 \cdot 10^{14} \text{ cm}^{-2}$ for CO₂ are obtained via equation (12) when $\psi = 0^\circ$. The column density values are in good agreement with those proposed by Kliore et al. [2002] for O₂ (ranging from $N_{O_2} = 3 \cdot 10^{16} \text{ cm}^{-2}$ to $N_{O_2} = 4 \cdot 10^{16} \text{ cm}^{-2}$), Vorburger et al. [2015] for O₂ ($N_{O_2} = 3 \cdot 10^{16} \text{ cm}^{-2}$), and Carlson [1999] for CO₂ ($N_{CO_2} = 8 \cdot 10^{14} \text{ cm}^{-2}$). For a comprehensive summary of atmospheric densities and compositions available in the literature, see Table 3.

Additionally, the asymmetric atmosphere model is consistent with observational data from Cunningham et al. [2015] who used Hubble Space Telescope observations to infer an atmospheric column density of $N_{O_2} = 4 \cdot 10^{15} \text{ cm}^{-2}$ in the wake and Jupiter-facing side of Callisto. Using equation (13), we are able to identify the location of the density value measured by Cunningham et al. [2015] in our model. In setting

$N_{O_2,\text{asym}} = 4 \cdot 10^{15} \text{ cm}^{-2}$ and $N_{O_2,0} = 2.3 \cdot 10^{16} \text{ cm}^{-2}$, an angle of $\psi = 160^\circ$ is obtained, which corresponds to the wakeside of Callisto and is thus qualitatively consistent with the observations from Cunningham *et al.* [2015]. Because the second atmosphere model exhibits axial symmetry with respect to the x axis, this column density value occurs anywhere along the circle defined by $\psi = 160^\circ$ in the wakeside hemisphere. Although a three-dimensional model of Callisto's atmosphere does not yet exist, the above method accounts for all available measurements of the neutral atmosphere to date (Table 3).

2.4. Model of Callisto's Ionosphere

The term ionosphere must be used with caution. Compared to Earth or Titan, the charged portion of Callisto's atmosphere is much more tenuous. However, in consistency with the literature, we refer to the charged particles that envelop Callisto as an ionosphere throughout the study.

Previous studies using A.I.K.E.F. have described, in detail, the technique for implementing an ionosphere within the model [see, for example, Kriegel *et al.*, 2009, 2011, 2014; Feyerabend *et al.*, 2015]. Therefore, only a brief description of the methods used to generate Callisto's ionosphere in the hybrid code is presented here. The procedures are the same as in the studies above, with relevant parameters adapted to the Callisto scenario.

2.4.1. Photoionization

To model the portion of Callisto's ionosphere generated by solar ultraviolet radiation, the solar EUV flux model for aeronomic calculations (EUVAC) is used [Richards *et al.*, 1994]. This model breaks up incoming flux from the Sun into 37 discrete wavelength bins from 50 to 1000 Å. Although more refined models of atmospheric ionization exist [see, for example, Richards *et al.*, 2006; Chamberlin *et al.*, 2007], EUVAC has successfully been implemented into the A.I.K.E.F. code and validated for photoionization at Titan [Feyerabend *et al.*, 2015]. Therefore, because of its proven applicability and to facilitate future comparisons between the two moons, this study continues to make use of this photoionization model. Because the values obtained from EUVAC are for Earth at a distance to the Sun of 1 AU, the incident flux must be scaled to the Sun-Callisto distance. This flux is subsequently used to calculate the photoionization production profile $P_{\text{pho},s}$ of neutral species $s \in \{\text{O}_2, \text{CO}_2\}$:

$$P_{\text{pho},s}(r) = n_s(r) \sum_{i=0}^{36} \sigma_{\text{ion},s}(\lambda_i) I(\lambda_i) \exp[-\tau_s(\lambda_i, r)] \quad , \quad (14)$$

where λ_i is the wavelength of the i th bin, $I(\lambda_i)$ is the flux at Callisto for each wavelength bin determined from the EUVAC model, and $\sigma_{\text{ion},s}(\lambda_i)$ are ionization cross sections for each atmospheric constituent, available in Appendix J of Schunk and Nagy [2009]. The optical depth $\tau_s(\lambda_i, r)$ at a certain position above the surface of Callisto is integrated along the line of sight from the Sun, represented by

$$\tau_s(\lambda_i, r) = \int_r^{\infty} \sum_s n_s(x) \sigma_{\text{abs},s}(\lambda_i) dx \quad , \quad (15)$$

where $\sigma_{\text{abs},s}(\lambda_i)$ are absorption cross sections for each atmospheric constituent [Schunk and Nagy, 2009]. For a combined O_2 and CO_2 atmosphere, the maximum photoionization production rates at the subsolar point are $P_{\text{pho},\text{O}_2} = 19.8 \text{ cm}^{-3} \text{ s}^{-1}$ and $P_{\text{pho},\text{CO}_2} = 0.895 \text{ cm}^{-3} \text{ s}^{-1}$, respectively. The use of an increased scale height (section 2.3) causes the local peak values to be 10 times lower than would be observed at Callisto.

This ionization procedure is valid for any configuration of the neutral atmosphere, regardless whether it exhibits symmetry or not. In using the symmetric atmosphere model (equation (11)), SUV radiation will generate a dayside ionosphere of equal strength independent of the orbital position of Callisto. However, the effectiveness of SUV radiation at a specific location is dependent on the neutral density of the atmosphere. Therefore, for the asymmetric atmosphere (equation (13)), photoionization is most effective when the ram-side hemisphere of the moon is also sunlit. This orientation occurs when Callisto is located at 18:00 LT, which corresponds to an alignment of corotating plasma and solar radiation (see Figure 1b). Alternatively, with an asymmetric atmosphere, photoionization is least effective when the wakeside of the moon is sunlit at 06:00 LT, which corresponds to an antialignment of the corotational plasma and incoming solar radiation. Jupiter shine may also play a similar role as solar EUV in ionizing Callisto's atmosphere but is not considered for this study.

2.4.2. Electron Impact Ionization

An additional source of ionization of the neutral atmosphere comes from collisions between magnetospheric electrons and atmospheric particles. To a first approximation, we assume isotropic impingement of energetic electrons onto the neutral atmosphere of the moon. Therefore, if the neutral atmosphere of Callisto is

symmetric, the portion of the ionosphere generated by electron impact is symmetric around the moon. For an asymmetric atmosphere, generation of an ionosphere from electron impact ionization is likewise asymmetric. Note, however, that unlike the ionospheric contribution from photoionization, electron impact ionization creates ionized particles on both the dayside and nightside hemispheres of the moon.

For this study, we consider electron energies between 300 and 1000 eV. In this temperature regime, the electron impact ionization rates were found to be nearly constant (see Seufert [2012, Figure 3.7] and discussion therein). Assuming an electron temperature of 635 eV, this author derived electron impact ionization rates of $k_{\text{imp}, \text{O}_2} = 1.04 \cdot 10^{-7} \text{ cm}^3 \text{ s}^{-1}$ and $k_{\text{imp}, \text{CO}_2} = 1.45 \cdot 10^{-7} \text{ cm}^3 \text{ s}^{-1}$ for O₂ and CO₂, respectively. To obtain a local ion production rate based on electron impact, the average background magnetospheric electron density of 0.1 cm⁻³ and local neutral density of each species are then multiplied by the rate to obtain ionospheric production values for O₂ and CO₂, consistent with the method introduced in Seufert [2012]. This leads to production rates that are approximately 2 times lower than production rates for photoionization, consistent with the findings of Seufert [2012]. It should be noted that the use of the average background magnetospheric electron density is only an approximation. In reality, the ionospheric production value due to electron impact would be affected by the perturbed electromagnetic fields near the moon. With that said, future studies may use the local—rather than averaged—electron density through inclusion of a higher-resolution simulation grid if needed.

2.4.3. Elastic Collisions

Also included in the ionosphere model are elastic collisions between charged and neutral particles. Within the hybrid model, these are carried out in a statistical manner as described in detail by Kriegel *et al.* [2011, 2014]. At each time step in the simulation, collision probabilities for individual particles are calculated to determine whether or not an ion collides with a neutral particle. The probability P^* that a collision has *not* taken place after a time t is given by

$$P^*(t) = \exp\left(-\frac{t}{\tau_{\text{col}}}\right) , \quad (16)$$

where τ_{col} is the average time between two collisions. The probability that a collision will occur in a given time interval is therefore $p\Delta t$, where

$$p = \frac{d}{dt} [1 - P^*(t)]_{t=0} = \frac{1}{\tau_{\text{col}}} = k_{\text{in}} n_s(r) . \quad (17)$$

Here k_{in} denotes the collision rate between an ion and a neutral and n_s the local neutral number density [Kriegel *et al.*, 2011, 2014].

In the simulation model, the product $p\Delta t$ is calculated for each ion during every time step and then compared against a random number $\xi \in [0, 1]$. If $p\Delta t < \xi$, no collision occurs. However, if $p\Delta t > \xi$, a collision occurs and the velocity of the charged particle is set to the velocity \mathbf{u}_s of the neutral species. Because $|\mathbf{u}_s| \approx 0 \ll |\mathbf{u}_i|$, this reduces the bulk velocity of the plasma. The elastic collision rates can be calculated as in Schunk and Nagy [2009] and Feyerabend *et al.* [2015] from

$$k_{\text{in}} = \frac{2.7 \cdot 10^{-9} (\alpha_s \mu_{\text{in}})^{0.5}}{m_i} , \quad (18)$$

where α_s is the neutral polarizability parameter for each neutral species [see Schunk and Nagy, 2009, Table 4.1] and μ_{in} is the reduced mass of the ion-neutral pair. Rates for the collisions considered in this study are as follows: $k_{\text{O}^+, \text{O}_2} = 6.64 \cdot 10^{-10} \text{ cm}^3 \text{ s}^{-1}$, $k_{\text{O}^+, \text{CO}_2} = 8.95 \cdot 10^{-10} \text{ cm}^3 \text{ s}^{-1}$, $k_{\text{O}_2^+, \text{O}_2} = 8.20 \cdot 10^{-10} \text{ cm}^3 \text{ s}^{-1}$, and $k_{\text{CO}_2^+, \text{CO}_2} = 2.39 \cdot 10^{-10} \text{ cm}^3 \text{ s}^{-1}$.

3. Modeling Results

3.1. Jovian Current Sheet Configuration

Parameters of the Jovian magnetospheric O⁺ ions as they impinge on Callisto when the moon is located at 18:00 LT and with an asymmetric atmospheric profile are presented in Figure 2. Callisto was located near this orbital position during three Galileo flybys (C20, C22, and C23; see Table 1), so the results for this local time are directly relevant for understanding the measurements obtained during those encounters. For Figure 2

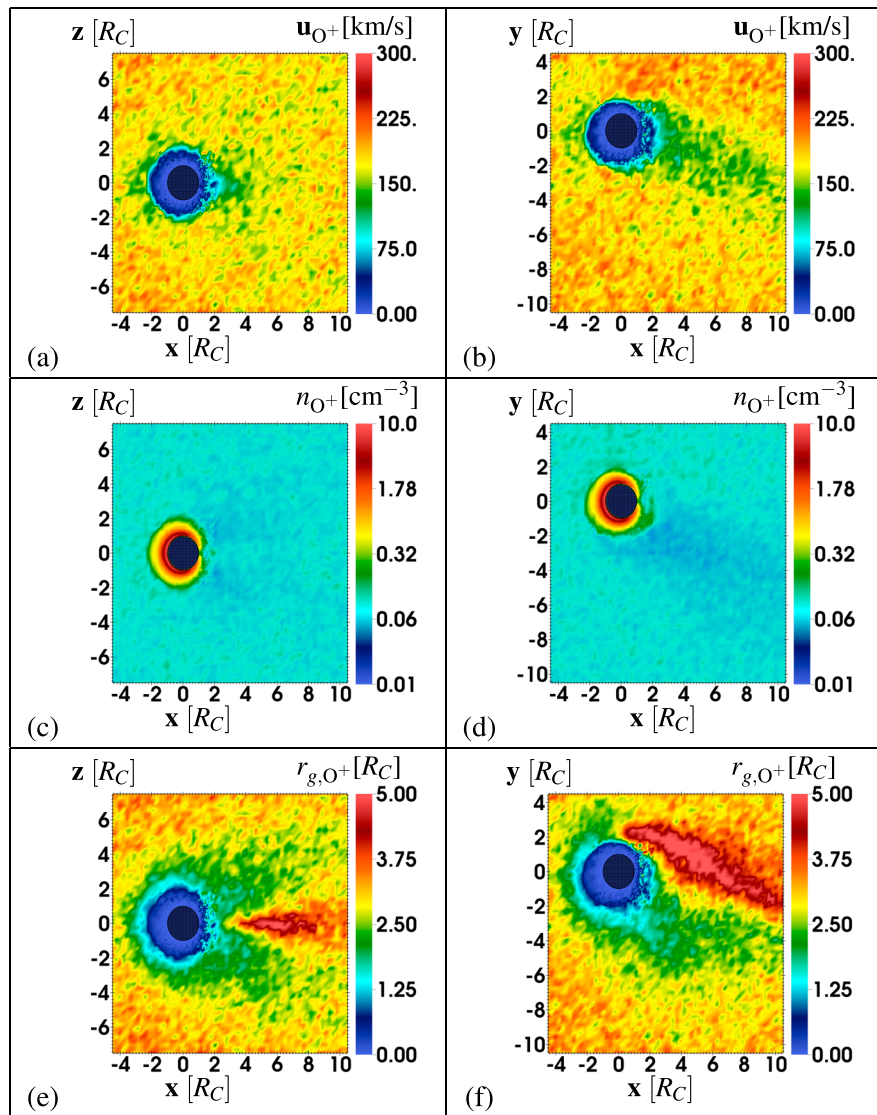


Figure 2. Jovian magnetospheric O^+ ion (a and b) bulk velocity, (c and d) number density, and (e and f) gyroradius ($r_g = \frac{m|\mathbf{u}_i|}{e|\mathbf{B}|}$) as it interacts with Callisto in the $y = 0$ (Figures 2a, 2c, and 2e) and $z = 0$ (Figures 2b, 2d, and 2f) planes, using the CphiO coordinate system.

and for the remainder of the study, the CphiO coordinate system is used. Figures 2a and 2b show the bulk velocity, Figures 2c and 2d the number density, and Figures 2e and 2f the gyroradii of the impinging magnetospheric O^+ ions. Figures 2a, 2c, and 2e display the quantities in the polar ($y = 0$) plane. This plane contains the undisturbed upstream ion bulk velocity vector \mathbf{u}_0 (along $\hat{\mathbf{x}}$) and the undisturbed magnetic field vector \mathbf{B}_0 (along $-\hat{\mathbf{z}}$). Figures 2b, 2d, and 2f display slices through the equatorial plane ($z = 0$) of the interaction region, containing the undisturbed upstream velocity vector \mathbf{u}_0 and the undisturbed convective electric field vector $\mathbf{E}_{c,0} = -\mathbf{u}_0 \times \mathbf{B}_0$ (along $-\hat{\mathbf{y}}$).

As plasma impinges on Callisto, the bulk velocity of the flow in the near vicinity of the moon is decreased as the plasma is mass loaded by ionospheric ions and deflected around the obstacle, as visible in Figures 2a and 2b. This corresponds to a density increase in the magnetospheric plasma on the ramside of Callisto on the order of approximately $10 \text{ cm}^{-3} = 100n_0$, visible in Figures 2c and 2d. The reduced bulk velocity and increased density cause a decrease in the average gyroradius ($r_g = \frac{m|\mathbf{u}_i|}{e|\mathbf{B}|}$) of the magnetospheric plasma from approximately $3R_C$ in the unperturbed plasma to $2R_C$ near Callisto. In the immediate vicinity of the moon where the velocity is almost stagnant, the gyroradius of the upstream plasma goes to zero (Figures 2e and 2f).

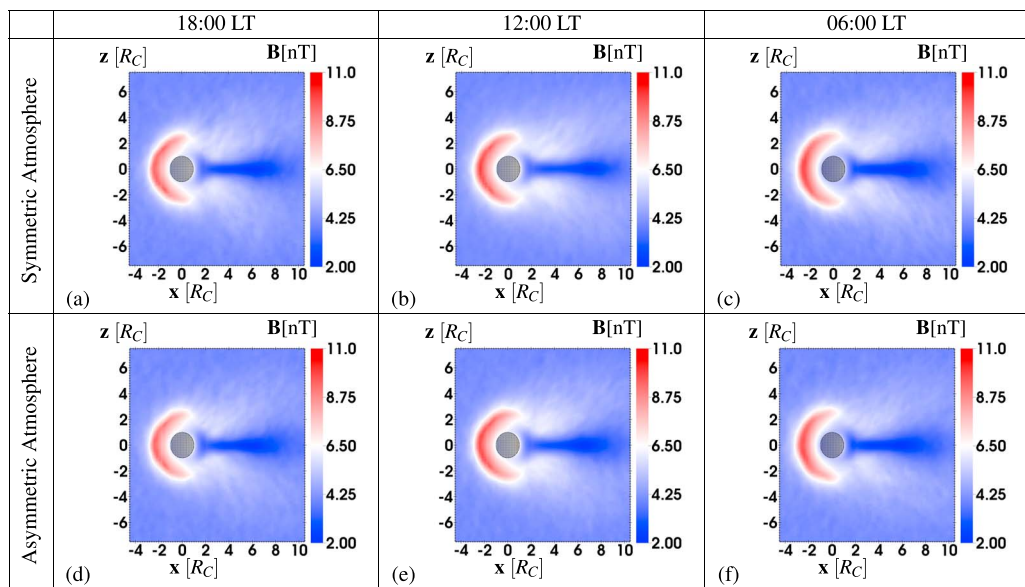


Figure 3. Total magnetic field strength in the $y = 0$ plane for (a–c) a symmetric atmosphere and (d–f) an asymmetric atmosphere around Callisto when located at 18:00 LT (Figures 3a and 3d), 12:00 LT (Figures 3b and 3e), and 06:00 LT (Figures 3c and 3f). The background field vector \mathbf{B}_0 is oriented along $-\hat{\mathbf{z}}$.

However, upstream of approximately $x = -3R_C$ and downstream beyond $x = 2R_C$, the gyroradius of the magnetospheric ions increases to again be much larger than the size of Callisto, i.e., to more than $1.25R_C$. In the polar plane at distances downstream larger than $x = 2R_C$, the magnetospheric velocity and number density return to their unperturbed states. However, the density and velocity depletions in the equatorial plane are much more extended, as perturbed regions persist beyond $x = 8R_C$ downstream of the moon. These regions exhibit asymmetries into the Jupiter-averted hemisphere.

The magnetospheric plasma perturbations exhibit only a minimal dependence on the location of Callisto's dayside ionosphere with respect to the impinging plasma. That is, the magnetospheric quantities display very similar behavior at 18:00, 12:00, and 06:00 LT. Due to the high thermal velocity of the incident magnetospheric plasma ($v_{th} \approx 212$ km/s) and the resultantly large value of the plasma beta, any changes in the magnetospheric flow patterns are readily smeared out by particle thermal motion. Therefore, the dependence of the magnetospheric flow structures on local time is rather weak. This finding is also consistent with our current understanding of Titan's plasma interaction. Similar to Callisto, Titan is embedded in a magnetosphere with a large plasma beta ($\beta \approx 10$), and various studies find the magnetospheric plasma flow pattern around Titan to be only weakly affected by Saturn local time [Simon et al., 2006, 2007; Ledvina et al., 2012]. Therefore, we do not show results from the 12:00 LT and 06:00 LT simulations for the Jovian magnetospheric plasma quantities.

3.1.1. Polar Plane

The magnetic field strength in the $y = 0$ plane for six different simulations is displayed in Figure 3. These correspond to simulations with a symmetric atmosphere in Figures 3a–3c and simulations with an asymmetric atmosphere in Figures 3d–3f, for 18:00 LT, 12:00 LT, and 06:00 LT (see Figure 1b for the various orbital positions of the moon with respect to impinging plasma and photoionization). On the ramside of the moon, the Callisto interaction region becomes visible at approximately $x = -3R_C$, with the region of largest magnetic pileup located near $x = -2R_C$. As the impinging magnetospheric plasma is decelerated near the moon, the magnetic field lines threading the plasma slow down as well and become trapped in the ionosphere of Callisto, resulting in pileup of the magnetic field. This pileup region is symmetric with respect to the $z = 0$ plane. The structure of the magnetic pileup is nearly identical for the different orbital positions of the moon considered in this study. In the region of largest pileup, a peak field strength of more than $2|\mathbf{B}_0|$ is reached. This value may be compared to the maximum strength of an induced magnetic field outside of the moon, which can be at most equal to $|\mathbf{B}_0|$ [Zimmer et al., 2000] or 4 nT for this setup. As such, induced magnetic field signals may be locally concealed by those arising from the magnetosphere-ionosphere interaction. Any flybys that occur

in or near the ramside hemisphere of Callisto when embedded in the weakly magnetized current sheet plasma would therefore not be suitable to unambiguously identify magnetic signals generated via induction in a subsurface ocean.

As with the ramside pileup region, the magnetic field in the wake is similar for each of the three orbital positions of Callisto shown. These simulations reveal a high level of robustness of the electromagnetic fields against changes in the location of the dayside ionosphere. A similarly robust behavior has been found to occur at Titan as well [Ledvina *et al.*, 2012]. As visible in the wakeside ($x > 0$) hemisphere of Callisto in each panel of Figure 3, the magnetospheric magnetic field is prevented from entering the equatorial tail downstream of the moon for any atmospheric configuration. A similar region of depleted magnetospheric field strength forms regardless of Callisto's distance to the center of the Jovian current sheet (see results presented in section 3.2). Therefore, close flybys through this region of minimal magnetospheric field are most suitable to detect induction signals from the moon's interior that are not contaminated by magnetic enhancements driven by the plasma interaction with Callisto's ionosphere or by the magnetospheric background field itself. While at large distances from Callisto, the induced field would be stretched into a magnetotail-like configuration (similar to the interaction of Mercury with the solar wind as in Benna *et al.* [2010]), directly downstream of the moon the unaltered induced field should dominate. For an alignment of the ambient magnetospheric field with the $-z$ axis, a close flyby through the wake of Callisto near $z = 0$ would be most suitable to detect such induction signals.

Any deviation from an entirely southward orientation of the background field would lead to a relocation of the area of reduced magnetospheric magnetic field. Such deviations become stronger with increasing distance of the moon to the center of the Jovian current sheet, where the field changes from a nearly antiparallel alignment with the z axis to a nearly parallel alignment with the $\pm y$ axis. A nonzero $B_{y,0}$ component would rotate the structures of the interaction region, including the region of reduced magnetospheric field in Callisto's tail, about the x axis. Additionally, a sweepback of magnetospheric field lines with respect to the strictly corotating meridional plane may generate a nonnegligible $B_{x,0}$ component of the magnetospheric field [Khurana and Kivelson, 1993], which would shift the region of reduced magnetic field to above or below the $z = 0$ plane. Simon and Motschmann [2009] studied the case of a nonzero $B_{x,0}$ component for Titan's plasma interaction and found that the neutral sheet does not remain flat but rather exhibits a curved structure. With the exception of the C9 flyby, all Galileo flybys of Callisto occurred in the moon's equatorial wake. Therefore, it is reasonable to assume that the region where the magnetospheric field is prevented from entering the moon's wake may have been missed by the spacecraft if a nonnegligible $B_{x,0}$ or $B_{y,0}$ were present. So while substantial induction signals may have been present at Callisto during each of the flybys, the identification of induction signals may be partially obscured depending on the trajectory of the flyby.

For future spacecraft missions, this result suggests that a precise model of the Jovian magnetospheric field at the orbit of Callisto is needed to determine the orientation of the background field before a flyby occurs. It would then be possible to choose a suitable inclination angle of the trajectory to aim for a close flyby through the region of reduced magnetospheric field strength in the moon's wake. In this way, one could see the induction signal in near isolation (barring any interconnection and coupling with other effects), regardless of the strength and the extent of the plasma interaction with an ionosphere.

In comparing the magnetic field perturbations for a symmetric (Figures 3a–3c) and asymmetric (Figures 3d–3f) atmosphere at a certain local time, no discernible differences in the interaction exist. Regardless of the orbital location of Callisto with respect to Jupiter, as long as there is an atmosphere with a column density of the same order as those proposed in the literature, the magnetic perturbations are similar both qualitatively and quantitatively for both types of atmosphere model considered here. For example, the peak value of the magnetic field in the pileup region is approximately 10 nT for all six simulations, with the crescent shape of the field enhancement nearly identical at each respective local time. In the wake, the magnetic field strength decreases to just above 2 nT for each local time and atmospheric configuration. The slight differences that do emerge from the different atmospheric configurations would probably not be measurable above the background fluctuations in the ambient magnetospheric field [cf. Kivelson *et al.*, 1999, Figure 4c].

With the result that the symmetric or asymmetric nature of the atmosphere has only minor quantitative impacts on the electromagnetic field perturbations near Callisto, it can be inferred that the fine structure of the atmospheric configuration plays only a minor role for quantifying the contribution of the magnetosphere-ionosphere interaction to Callisto's complex, entangled magnetic environment.

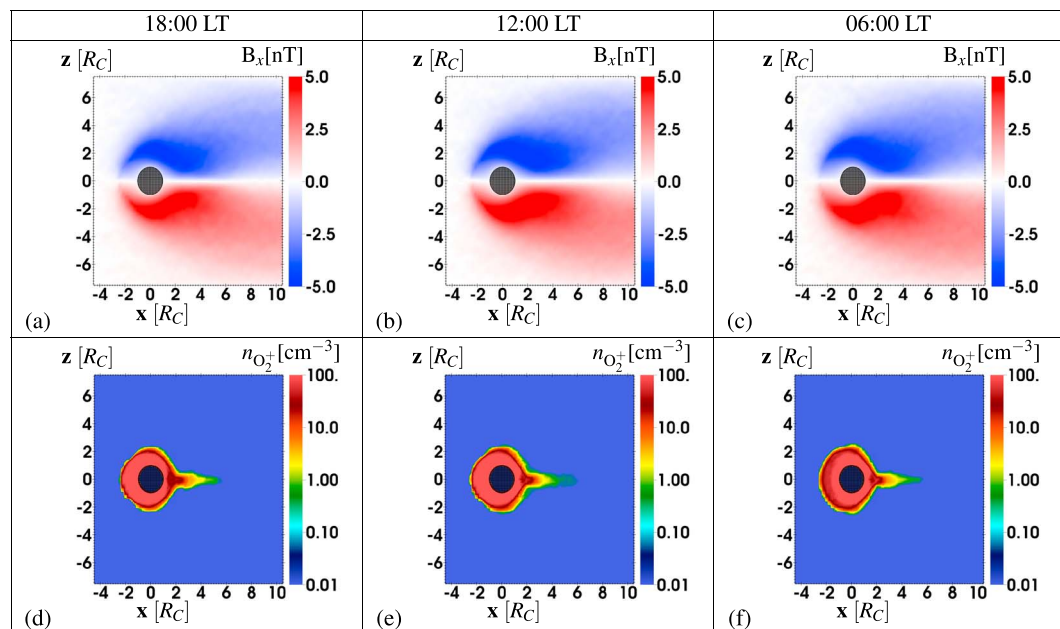


Figure 4. The (a–c) x component of the magnetic field B_x and (d–f) ionospheric O_2^+ plasma number density in the $y = 0$ plane for an asymmetric atmosphere at the same times as Figure 3.

This result holds true for all flybys of Callisto that occur far outside of the moon's atmosphere. Except for the C30 flyby, the closest approaches of all Galileo flybys occurred near or well above 500 km (Table 1). These distances correspond to more than two of the atmospheric scale heights used throughout this study. Even with the increased scale heights, any changes in the structure of the atmosphere would occur on scales that are on the order of $0.1R_C$ and would only have a weak influence on the structure of the large-scale magnetic field perturbations that occur on scales of $1–10R_C$. The impact of different atmospheric configurations is even more subtle in reality, as the actual scale height is a factor of 10 less than the one used here, so changes of the atmosphere would occur on scales less than $0.01R_C$. Therefore, throughout the remainder of this study, only results for Callisto with an asymmetric atmospheric configuration, as suggested by Kliore et al. [2002] and consistent with Cunningham et al. [2015], will be presented. We would like to note, however, that for any future flybys that occur through Callisto's atmosphere (i.e., with closest approach altitudes on the order of 100 km), the impact of varying atmospheric configurations would possibly be visible in magnetic field data.

We now seek to further constrain the magnetosphere-ionosphere interaction at Callisto as a function of local time. Figures 4a–4c show, from left to right and for an asymmetric atmosphere, the B_x component of the magnetic field in the $y = 0$ plane at 18:00 LT, 12:00 LT, and 06:00 LT. The two Alfvén wings are visible at an angle $\theta = 70^\circ$ against the background field, corresponding to an Alfvénic Mach number of $M_A = \tan \theta = 2.8$ (for $\mathbf{u}_0 \perp \mathbf{B}_0$), [cf. Neubauer, 1980]. The structure of the Alfvén wings is nearly unaffected by the orbital position of the moon, as the quantitative perturbations in B_x are nearly the same for each local time. As in Figure 3, the magnetic perturbations are symmetric with respect to the $z = 0$ plane.

Figures 4d–4f display the number density of ionospheric O_2^+ pickup ions at the same local times as above in the $y = 0$ plane (containing \mathbf{B}_0 and \mathbf{u}_0). Since the density of ionospheric CO_2^+ is more than an order of magnitude smaller than the ionospheric O_2^+ density, the CO_2^+ ions essentially act as test particles and do not have a noticeable impact on the electromagnetic fields. Therefore, figures displaying CO_2^+ quantities are not shown here. Similar to the magnetic field perturbations in the $y = 0$ plane, the region of increased O_2^+ density is nearly symmetric with respect to $z = 0$. At distances larger than $x = 2R_C$, the pickup ion density enhancement is confined to the neutral sheet between Callisto's magnetic lobes (i.e., $\pm 0.5R_C$ along the z axis), where the magnetic pressure is low. In other words, Callisto's pickup tail exhibits a flat structure. Flybys of the moon that occur above or below this flat tail would not see any density enhancement in the ion population associated with Callisto. Additionally, the pickup tail appears to abruptly end near $x = 5R_C$. The reason for this density cutoff will become clear in section 3.1.2.

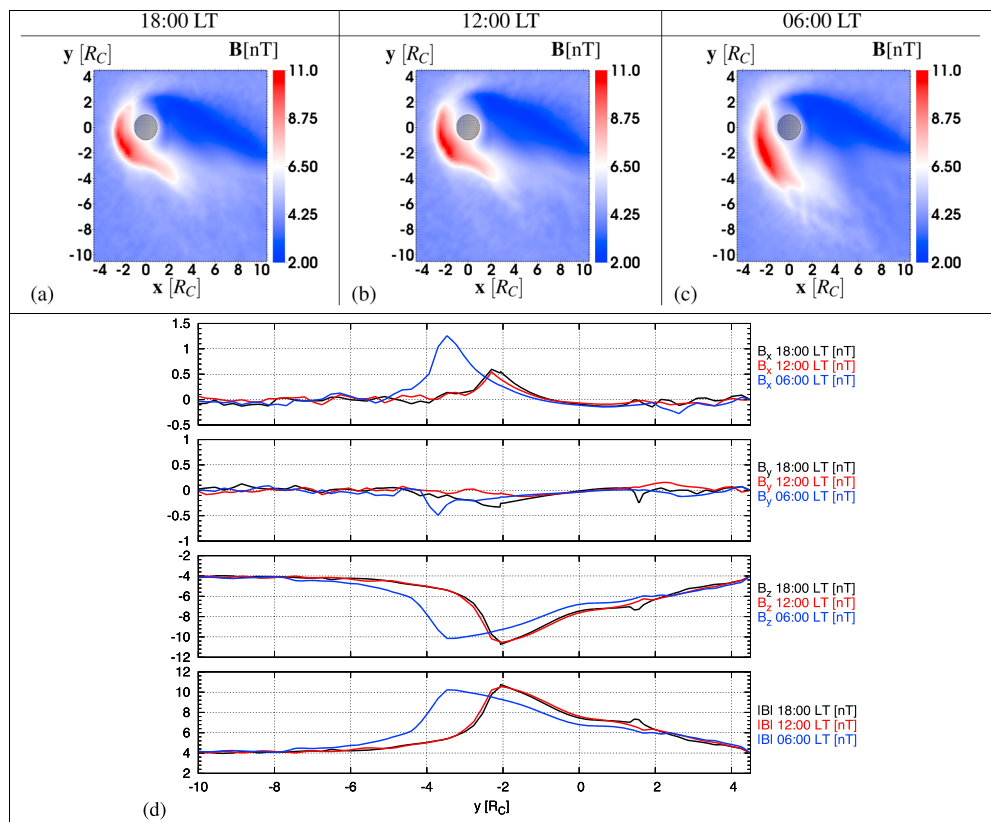


Figure 5. (a–c) Total magnetic field strength in the $z = 0$ plane at the three local times presented in the study. (d) B_x , B_y , B_z , and $|\mathbf{B}|$ for a trajectory along the y axis at $x = -1.5R_C$ and $z = 0R_C$ when Callisto is located at 18:00 (black), 12:00 (red), and 06:00 (blue) local times.

3.1.2. Equatorial Plane

The total magnetic field in the $z = 0$ plane for the three orbital positions is shown in Figures 5a–5c. This is also the plane that contains both the undisturbed convective electric field \mathbf{E}_0 (aligned with $-\hat{\mathbf{y}}$) and the corotational bulk velocity vector \mathbf{u}_0 (aligned with $\hat{\mathbf{x}}$). Because the model treats ions kinetically, this study resolves magnetic field asymmetries driven by the large gyroradii of the pickup ions (see Table 2) in the plane perpendicular to the magnetic field. In this plane, the pickup ions move on cycloidal trajectories with the open sides of the cycloidal arcs facing Jupiter. Due to the large gyroradii of the pickup ions ($r_{g,O_2^+} = 6.61R_C$), the magnetic pileup region and the magnetic cavity are both shifted into the Jupiter-averted half-space ($y < 0$). The distance between two subsequent turning points of each O_2^+ cycloid is approximately $\Delta x = 2\pi r_g = 41.5R_C$, and the particles reach a maximum distance to the $y = 0$ plane of $\Delta y = 2r_g = 13.2R_C$ (see Simon et al. [2007] for derivation of these equations). Slight variations in the magnetic field structure generated by changes of Callisto's orbital position are visible. When located at 18:00 LT and 12:00 LT, the region of magnetic field buildup strongly wraps around the moon in the anti-Jovian half-space, whereas at 06:00 LT, this structure is far less curved and still visible at $y = -5R_C$ compared to $y = -3R_C$ for the 18:00 and 12:00 LT simulations. Simon et al. [2007] investigated Titan's plasma environment at various local times and found that the magnetic field shows a similar behavior.

To better illustrate the dependency of the magnetic field signatures on Callisto's orbital position, Figure 5d displays the magnetic field components along a cut through Callisto's ramside magnetic barrier at $x = -1.5R_C$ for the three local times simulated in this study. The peak value of B_x at 06:00 LT (represented by the blue line in the figure) is enhanced by approximately 0.7 nT and displaced into the Jupiter-averted hemisphere by more than $1R_C$ compared to at 18:00 and 12:00 LT (in black and red), while B_z is diminished by 1 nT and displaced by more than $1R_C$ into the Jupiter-averted hemisphere compared to the other two local times.

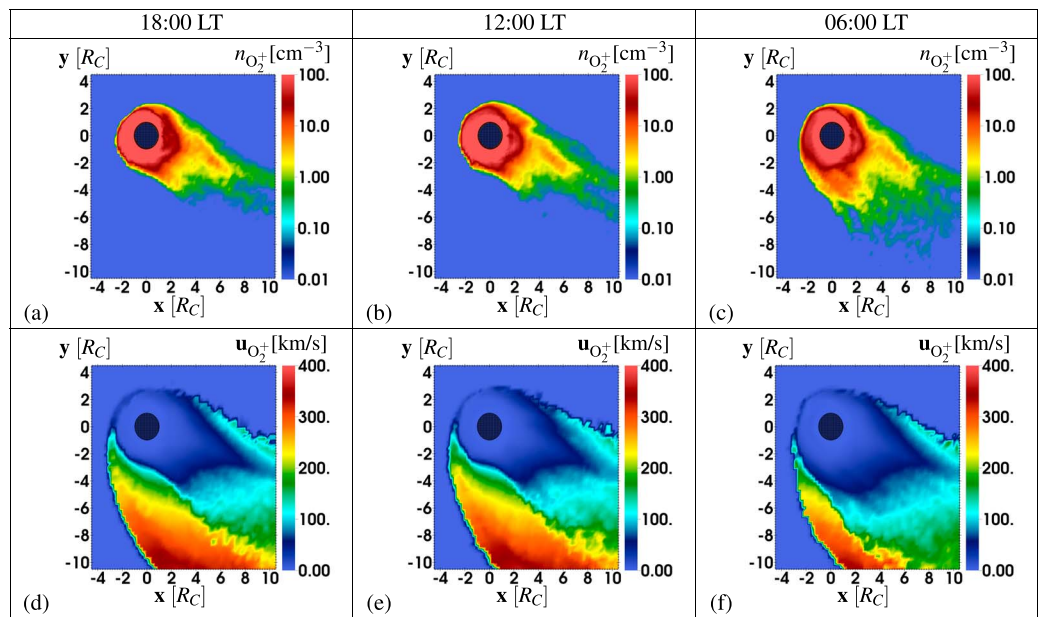


Figure 6. (a–c) Ionospheric O_2^+ pickup ion number density in the $z = 0$ plane. The color bar for the density values is oversaturated to highlight the less dense tail structures at large distances ($> 2R_C$) from the surface of Callisto. (d–f) Bulk velocity of the O_2^+ pickup ions, with $\max|\mathbf{u}| \approx 2|\mathbf{u}_0|$.

However, these slight differences that arise due to the local time may not be observable by a spacecraft over magnetospheric background “jitters” in the magnetic field that are not related to Callisto such as those visible in Figure 4c of Kivelson *et al.* [1999].

Figures 6a–6c show the pickup ion number density of O_2^+ in the $z = 0$ plane. For all three local times shown, an asymmetric tail structure with respect to the $y = 0$ plane forms due to the large gyroradii of the pickup ions. This asymmetric pickup tail extends far into the Jupiter-averted half-space. Beyond approximately $x = 5R_C$, the entirety of the pickup tail is located in the $y < 0$ half-space, and beyond approximately $x = 6R_C$, Callisto’s pickup tail is shifted out of the moon’s geometric shadow due to the large ion gyroradii. For this reason, the ion tail appears to abruptly end in the polar plane, as was visible in Figures 4d–4f. Similar effects have been found at Titan [Simon *et al.*, 2007; Feyerabend *et al.*, 2015], Mars [Bößwetter *et al.*, 2004], and comets [Bagdonat, 2005]. The newly generated ions escape along cycloidal trajectories that extend well out of the simulation domain. The large gyroradius of the pickup ions (visible in the O_2^+ pickup ion velocity displayed in Figures 6d–6f) causes the upstream flank of the pickup tail to be perpendicular to the direction of corotational flow over more than $5R_C$. This effect also occurs at weak comets: at large heliocentric distances, the cometary pickup tail is perpendicular to the Sun-comet line and not transported radially by the solar wind [Bagdonat, 2005].

At 18:00 LT (Figure 6a), when incoming SUV radiation and corotation are aligned, the majority of the newly generated ions on the ramside of the moon must convect completely around Callisto and are then lost into the tail. The density increase in the tail near $1R_C < x < 2R_C$ is on the order of 100 cm^{-3} , which is more than 10 times the density increase of the magnetospheric density in the same region between $x = 1R_C$ and $x = 2R_C$. The corresponding O_2^+ pickup ion velocity plot for 18:00 LT (Figure 6d) shows that the pickup tail is much more extended away from Jupiter than is visible in the density signature. The velocity of the pickup ions is limited to approximately twice the magnetospheric background velocity $|\mathbf{u}_0|$ [Simon *et al.*, 2007], and this value is nearly reached here at the edge of the simulation domain as the ions are accelerated over half of a gyration period in approximately 261 s. The region of low velocity in Callisto’s wake corresponds to the region of increased pickup ion density. For the simulation with Callisto located at 12:00 LT, i.e., with solar ionization aligned with the $+y$ direction and thus impinging on Callisto’s Jupiter-averted hemisphere, both the density (Figure 6b) and bulk velocity (Figure 6e) patterns of the O_2^+ pickup ion species are qualitatively similar to the structures that occur at 18:00 LT. The simulation at 12:00 LT reveals only minor quantitative differences compared to the interaction at 18:00 LT.

However, when photoionization and corotation are antialigned at 06:00 LT, the structure of the tail is noticeably different. The number density and bulk velocity of O_2^+ for this orbital position are shown in Figures 6c and 6f. A second escape channel of enhanced density arises in the Jupiter-averted half-space near $x = 2R_C$ compared to the 18:00 LT and 12:00 LT cases. In the wake of the moon, increased O_2^+ pickup ion densities are also identified at 06:00 LT. This subtle increase arises from the location of the wakeside hemisphere with respect to incoming solar radiation. As photoionization is maximized on the wakeside of the moon, the majority of ions do not need to convect around Callisto. This allows for a denser ionospheric population to accumulate in the wake compared to other orbital positions. Furthermore, the ions are injected into a region of reduced magnetic field compared to the background value (see Figures 5a–5c). Therefore, many of the ions initially become “trapped” in Callisto’s tail, as the electromagnetic fields are not able to efficiently pick up the particles. Figure 6f shows the effect of the increased pickup ion density in the tail more clearly, where the region of high velocity (depicted in red) for O_2^+ ions is much narrower for $-4R_C < y < -10R_C$. Additionally, the region of low pickup velocities at values less than $|\mathbf{u}_0|$ (depicted in blues and greens) has grown at the expense of the region with velocity values larger than $|\mathbf{u}_0|$. This process is the cause of the “unwrapping” of the magnetic pileup region at 06:00 LT compared to 18:00 LT and 12:00 LT (Figures 5a–5c). The decreased velocity at the Jupiter-averted flank of the moon prevents the magnetic field from penetrating deeply into the wake of Callisto as it does at 18:00 and 12:00 LT.

Whereas only a slight dependence on local time is visible in the magnetic field structure, the number density and especially the bulk velocities of the pickup ions are highly affected by the orbital position of the moon. This is further seen in the fine structure of the density in the pickup tail. As shown in Figure 6, a wakeside density increase on the order of 100 cm^{-3} is visible in the immediate vicinity of the moon for all three local times. Further in the wake beginning around $x = 3R_C$, a single filament of increased density extends into the anti-Jovian hemisphere of Callisto for the three local times shown. At 06:00 LT, a second filament is visible farther from the moon beginning near $y = -4R_C$ and extending downstream, marked by a number density increase by more than a factor of 10 (depicted in orange and red hues). This structure is not present when the moon is located at 18:00 or 12:00 LT. The split tail structure in the ion density of Callisto’s plasma wake is similar to a process that spawns from Titan’s ionospheric interaction with the Saturnian magnetospheric plasma. Filamentation in Titan’s ion pickup tail has been measured by the Cassini Plasma Spectrometer during the T9, T63, and T75 tail crossings [Coates et al., 2012]. These structures have been modeled with a hybrid approach by Feyerabend et al. [2015].

The high density of slow ionospheric particles is responsible for partially shielding the O_2^+ ions from pickup by the magnetospheric electromagnetic fields. As freshly ionized particles move into the wake of Callisto, the density of slow ionospheric particles in the tail is more than an order of magnitude larger than the magnetospheric O^+ number density in the same region. This accumulation of a low-speed population reduces the bulk velocity of the ions, represented by

$$\mathbf{u}_i = \frac{n_{\text{ms}}}{n_{\text{ms}} + n_{\text{is}}} \mathbf{u}_{\text{ms}} + \frac{n_{\text{is}}}{n_{\text{ms}} + n_{\text{is}}} \mathbf{u}_{\text{is}} , \quad (19)$$

where subscripts ms and is correspond to magnetospheric and ionospheric ions, respectively. The decrease of \mathbf{u}_i in the tail reduces the convective electric field

$$\mathbf{E}_c = -\mathbf{u}_i \times \mathbf{B} \quad (20)$$

which is represented by the first term on the right-hand side of equation (7). This partially prevents further pickup of the tail ions by the magnetospheric electric field. Then, because of the reduced bulk velocity of the plasma, the continuity equation requires the plasma density to increase further, thereby reducing the convective electric field even more. In this manner, the ions in the tail partially shield themselves from the electromagnetic fields generated by the plasma interaction. This process is most effective at 06:00 LT, when ions produced by photoionization can directly fill Callisto’s wake and the density of ionospheric particles in the tail is maximized, but is present at 18:00 and 12:00 LT as well.

Similar effects occur at other solar system bodies. The density of pickup ions in the tail of Titan is controlled by a positive feedback loop arising from the mechanism described above. The densest “core region” of Titan’s tail shields itself from pickup by the ambient electromagnetic fields [Simon et al., 2008]. At weak comets, this feedback mechanism manifests in the form of a heavy ion density jump at the outer boundary of the interaction region, where increased heavy ion densities reduce the pickup efficiency of the electric field

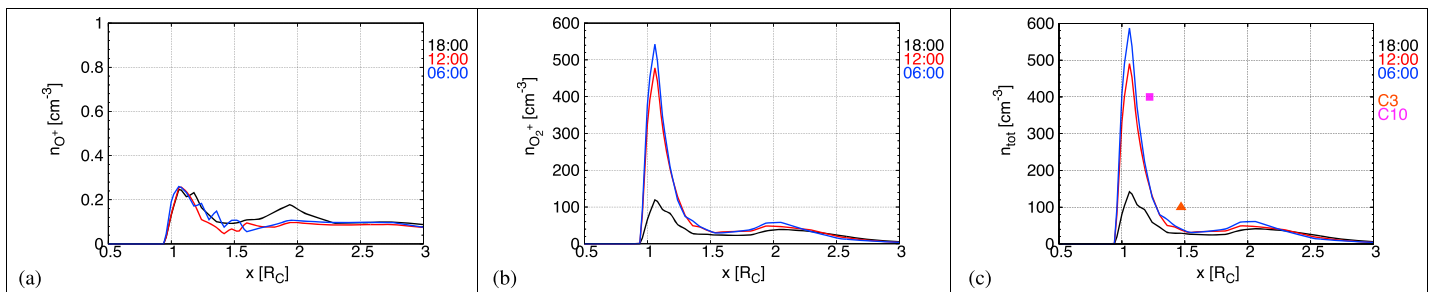


Figure 7. (a) Magnetospheric O⁺ density, (b) ionospheric O₂⁺ density, and (c) total ion/electron number density in the wake of Callisto along the x axis at 18:00 (black), 12:00 (red), and 06:00 (blue) LT. The maximum electron density values at the altitude of closest approach from the C3 (orange triangle) and C10 (pink square) flybys are included as well. Note the much lower maximum density value and axis range in Figure 7a compared to Figures 7b and 7c. The background magnetospheric density is set to $n_0 = 0.1 \text{ cm}^{-3}$.

[Bagdonat, 2005]. That study also noted the analogy between this shielding and that of the electric field in a Faraday cage. Whether at Callisto, Titan, or weak comets, this mechanism is purely kinetic and can only be resolved through simulations that treat the pickup ions as individual particles.

To more clearly illustrate the differences in density, Figure 7 shows the density of (a) the O⁺ magnetospheric ions, (b) O₂⁺ ionospheric ions, and (c) the total ion density in the wake along the x axis, which includes the sum of O⁺, CO₂⁺, and O₂⁺ ions. Each line corresponds to a different local time: 18:00 (black), 12:00 (red), or 06:00 (blue) LT. Note that number density is zero for $|x| < 1R_C$, as this corresponds to locations beneath the surface of the moon, and the slight density visible below $1R_C$ is due to the finite cell size in the simulation domain. For the upstream plasma (Figure 7a), an increase of approximately $2n_0$ to 0.25 cm^{-3} is seen near the surface in Callisto's wake. Approximately $0.5R_C$ downstream, this enhancement returns to the background value. Figure 7b shows that the ionospheric O₂⁺ pickup ion density in the tail of the moon increases to more than $1000n_0$.

In comparing Figures 7b and 7c, the O₂⁺ density clearly dominates the pickup ion population in the tail. At 06:00 LT, a maximum total ion (Figure 7c) density increase to nearly 600 cm^{-3} is seen. Since we assume quasi-neutrality, the ion densities shown here also represent the total electron number density along this artificial trajectory and can be directly compared to the maximum electron number density values measured by the plasma wave instrument on Galileo during flybys of Callisto [Gurnett et al., 1992]. Because the C3 and C10 flybys occurred near 06:00 LT and in Callisto's wake, the wakeside density values at 06:00 LT can be directly compared to measurements in Gurnett et al. [1997, 2000] for the two flybys, represented in Figure 7c by an orange triangle for the C3 flyby and by a pink square for the C10 flyby. Gurnett et al. [1997, 2000] found plasma densities of 100 cm^{-3} for C3 and 400 cm^{-3} for C10, which is of the same order of magnitude as the values seen here. A magnetospheric number density increase in the moon's wake to a value of 0.25 cm^{-3} is unable to explain the much stronger electron density enhancement of $100\text{--}400 \text{ cm}^{-3}$ measured by Galileo flybys. These density values are only matched through inclusion of an atmosphere, emphasizing the important role of Callisto's atmosphere and ionosphere in its interaction.

3.2. Jovian Lobe Configuration

When Callisto is located in one of the lobes of the Jovian magnetodisk, i.e., in regions where the field lines are radially stretched and compressed, the magnetic field strength encountered by the moon can be nearly an order of magnitude larger than in the current sheet. To study the plasma interaction under these magnetospheric conditions, results are presented with the use of $|\mathbf{B}_0| = 40 \text{ nT}$ [see, for example, Neubauer, 1998; Kivelson et al., 2004]. This magnetic field strength increase reduces the size of the ion gyroradii by an order of magnitude (displayed in Table 2), leading to a much more symmetric structure of the interaction region.

As previously mentioned, \mathbf{B}_0 remains aligned along $-\hat{\mathbf{z}}$ to facilitate comparison with results in section 3.1. Although the ionosphere is expected to have less of an effect on the plasma interaction at this location [cf. Zimmer et al., 2000], the contribution of the ionosphere still affects the overall entangled interaction scenario at Callisto. It is therefore important to understand the extent to which the magnetic field and plasma perturbations are driven by the interaction with Callisto's ionosphere. As shown in section 3.1 when the moon is embedded in the Jovian current sheet, the electromagnetic field perturbations generated by the plasma interaction with Callisto's ionosphere are nearly independent of the solar phase angle. The impact of the angle between the direction of photoionization and corotation is even weaker with an increased background

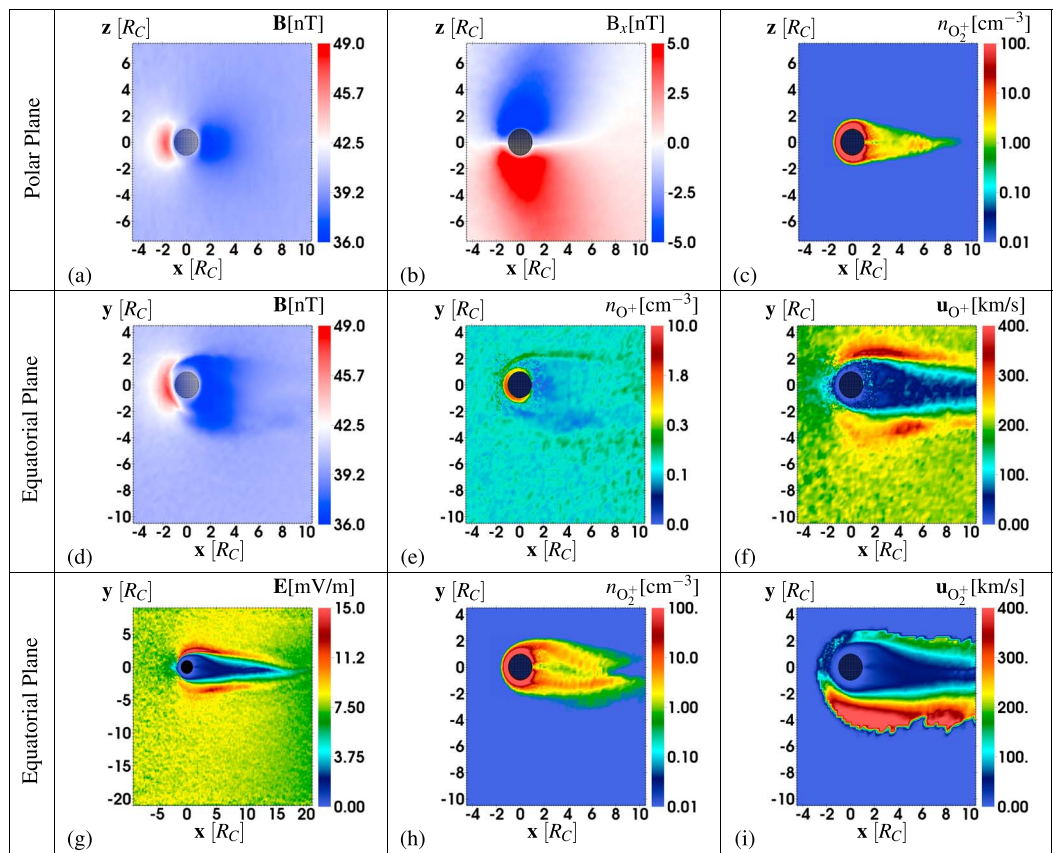


Figure 8. For the case of Callisto embedded in one of the magnetodisk lobes of Jupiter with $\mathbf{B}_0 = -40\hat{\mathbf{z}}$ nT: electromagnetic and plasma quantities in the $y = 0$ plane displaying (a) total magnetic field magnitude $|\mathbf{B}|$, (b) the magnetic field component B_x , and (c) number density of ionospheric O_2^+ pickup ions. Electromagnetic and plasma quantities in the $z = 0$ plane for (d) total magnetic field magnitude $|\mathbf{B}|$, (e) magnetosospheric O^+ number density, (f) magnetosospheric O^+ bulk velocity, (g) total electric field magnitude $|\mathbf{E}|$ for the entire simulation domain, (h) ionospheric O_2^+ number density, and (i) ionospheric O_2^+ bulk velocity.

magnetic field because the “stiffness” of the magnetic field lines is increased; i.e., it is harder to drape the magnetospheric field around the moon. We therefore focus only on the 18:00 LT case, as the interactions that occur at 12:00 and 06:00 LT exhibit very similar behavior.

Figure 8 presents the interaction of Callisto with the Jovian magnetospheric plasma when embedded in one of the magnetodisk lobes. Figures 8a–8c show a polar ($y = 0$) slice through the interaction region, whereas Figures 8d–8i display an equatorial ($z = 0$) slice, all at 18:00 local time (corresponding to $\alpha_{\odot} = 270^\circ$). The total magnetic field magnitude in the $y = 0$ plane is plotted in Figure 8a. Similar to the current sheet cases, a pileup region begins to form upstream at approximately $x = -3R_C$, with a peak field enhancement of approximately 8 nT. The reduced inclination of the Alfvén wing prevents the magnetic field from wrapping around Callisto as strongly as in the Jovian current sheet. Therefore, the crescent structure of the ramside magnetic perturbation is far less pronounced here. Downstream of Callisto, the field decreases in strength by nearly 4 nT compared to the background field. Figure 8b shows the Alfvén wing at an angle of 15° clearly visible in B_x much beyond the regions where the magnetic field magnitude is perturbed. Similar to the current sheet simulations, the perturbations in the magnetic field are symmetric with respect to $z = 0$ in this plane.

In examining the magnetic field in the equatorial pickup plane (Figure 8d), we see that the perturbations are nearly symmetric about $y = 0$ as well. There is a slight asymmetry where the pileup region extends into the $y < 0$ half-space to $y = -2R_C$, but the expansion of the magnetic pileup into the $y < 0$ half-space that was present in the current sheet case has almost disappeared. This is due to the much smaller gyroradii of the ionospheric pickup species. For the wake, Figure 8d shows that the area of reduced magnetic field exhibits an

asymmetric pattern, as the region of reduced field extends to $y = -4R_C$ in the $y < 0$ hemisphere but only to $y = 2R_C$ in the $y > 0$ hemisphere. When the moon is located near the center of the Jovian current sheet, this asymmetry is much more pronounced (see Figures 5a–5c).

When Callisto is embedded in the Jovian current sheet, the peak perturbation in the magnetic field, $\Delta|\mathbf{B}| = |\mathbf{B}| - |\mathbf{B}_0|$, is approximately 6 nT (e.g., Figure 3). Similarly, when located in one of Jupiter's magnetodisk lobes, the maximum value of the perturbation to the background magnetic field is on the order of 8 nT. However, the relative value of the perturbation is $\frac{\Delta|\mathbf{B}|}{|\mathbf{B}_0|} \approx 1.5$ in the current sheet, whereas for the lobe scenario, $\frac{\Delta|\mathbf{B}|}{|\mathbf{B}_0|} \approx 0.2$. This result is of paramount importance for disentangling magnetic signals generated by a combination of the magnetosphere-ionosphere interaction, magnetosphere-dipole interaction, and induced magnetic fields.

When Callisto is located far from the center of the Jovian current sheet, the signal generated by the magnetosphere-ionosphere interaction alone is still on the order of 20% of the background field. So although induction signals may dominate in this scenario, a nonnegligible portion of the magnetic perturbations may still be generated by the magnetosphere-ionosphere interaction. Therefore, the ionospheric contribution to the perturbed electromagnetic fields needs to be taken into account when investigating the magnetic field in flyby data near the moon. This finding is consistent with Strobel *et al.* [2002].

As with the symmetry of the current sheet scenarios in the $y = 0$ plane, the number density for the ionospheric O_2^+ is symmetric in the $y = 0$ plane about the z axis (Figure 8c). On the ramside of the moon, while the peak density value remains consistent with the Jovian current sheet scenario (e.g., Figure 4d), the region of enhanced ion density is confined closer to Callisto's surface for the lobe scenario. The O_2^+ density increase extends to only $x = -2R_C$ upstream, as the increased ambient magnetic field restricts the ionosphere from further expansion toward upstream. In the wake, where a cutoff of the tail was visible when the moon was embedded in the Jovian current sheet (e.g., Figure 4d), a symmetric cone-like region of enhanced ion density is formed in the lobe scenario. This structure is caused by the decreased inclination of the Alfvén wings which broadens the region of reduced magnetic field. Thus, the region of reduced magnetic pressure into which the pickup ions can expand is enlarged, and a broader tail is formed. The wider structure of the pickup tail suggests that detection of increased ion density in Callisto's wake by a spacecraft would be easier as the tail is not as "flat" compared to the current sheet scenario. Additionally, the tail remains in the $y = 0$ plane (i.e., is not bent out of this plane by gyration of ionospheric pickup ions) further downstream compared to the current sheet scenario. The pickup tail is finally shifted out of this plane at $x = 8R_C$ (cf. Figure 8h).

For the $z = 0$ plane, Figure 8e displays the perturbation in the number density of the magnetospheric O^+ ions as they interact with Callisto. A region of enhanced O^+ density is visible at the ramside of Callisto and the flanks of the interaction region as the plasma is diverted around the moon in a nearly symmetric manner. This overall symmetric structure is also visible in Figure 8f, which shows the velocity of the magnetospheric O^+ ions. At the sides of the moon where the ions are deflected around Callisto, velocity enhancements to nearly twice the upstream velocity can be identified in both the $y < 0$ and $y > 0$ hemispheres. The deflection is much more symmetric than in the current sheet situation (Figure 2). Slightly asymmetric patterns are still visible, especially in the density increase near the surface of the moon that is more pronounced in the $y < 0$ hemisphere. This suggests that the nonnegligible ion gyroradii are still important. Finally, the magnetospheric density in the wake is reduced to below the background value of 0.1 cm^{-3} . This echoes a result of the current sheet scenario. To explain the electron density enhancements in Callisto's wake for flybys C3 and C10 [see Gurnett *et al.*, 1997, 2000], an atmosphere surrounding the moon must be present. Increases in the magnetospheric O^+ plasma density alone are not sufficient to explain the density increase by 2 orders of magnitude.

Similar to the upstream number density, the overall structure of the ionospheric O_2^+ number density perturbation displayed in Figure 8h is rather symmetric with respect to the $y = 0$ plane. Only the fine structure of the ionospheric O_2^+ density displays asymmetries. To a much larger degree than in the current sheet scenario (see Figure 6c), a filamented ion tail is formed downstream of Callisto. The escaping pickup ions are mainly confined to two tube-like channels of increased density, each possessing a thickness of approximately $1R_C$. The filament in the $y > 0$ hemisphere is bent slightly toward the $y = 0$ plane, while the filament in the $y < 0$ hemisphere is more aligned with the direction of corotation and is longer than its counterpart, extending approximately $8R_C$ downstream.

As can be seen from Figure 8i, the flow pattern of the ionospheric O_2^+ ions is strongly asymmetric. Similar to the scenario of Callisto located in the Jovian current sheet, the ions are picked up by the electromagnetic fields and accelerated over half of a gyration period (approximately 26.1 s) into the $y < 0$ half-space. Again, the cycloidal structure of the pickup tail is visible in the bulk velocity pattern, with the pickup velocity largest near the turning points of the cycloidal arcs. These arcs are an order of magnitude smaller compared to the current sheet scenario but are still comparable to the size of Callisto, with $\Delta x = 2\pi r_g = 4.15R_C$ and $\Delta y = 2r_g = 1.32R_C$ for ionospheric O_2^+ . Thus, even when Callisto is located in the lobes of Jupiter's magnetodisk, the study of its plasma interaction requires a kinetic treatment of the ions.

The extension of Callisto's interaction region in the plane perpendicular to the background magnetic field is visible in Figure 8g, which shows the electric field (equation (7)). In contrast to the other panels of Figure 8, this panel displays the entire simulation domain that extends from $-9R_C \leq x \leq 21R_C$ and $-21R_C \leq y \leq 9R_C$. In this plane, Callisto's interaction region extends approximately $20R_C$ downstream of the moon, characterized by a cavity where the electric field is drastically reduced compared to the background value. This region corresponds to the regions of reduced flow velocities (see Figures 8f and 8i) of the magnetospheric and ionospheric species. A large-scale symmetry in the perturbed electric field is visible with the persistence of smaller asymmetric features.

The results of this simulation confirm the findings of Strobel *et al.* [2002], who suggest large-scale deflection of Jupiter's magnetospheric plasma around Callisto due to interaction with its ionosphere alone. These authors analytically solve for a plasma bulk velocity on the order of 0.1 km s^{-1} . Although here the minimum bulk velocities of magnetospheric O^+ (Figure 8f) and ionospheric O_2^+ (Figure 8i) ions are on the order of 1 km s^{-1} , the velocity values near the moon in this study are consistent with a substantial deceleration of the ambient flow. Strobel *et al.* [2002] were unable to discriminate between magnetospheric and ionospheric ions, but both species reduce to a similar velocity near Callisto. Additionally, the analytical solution to the ratio of the electric field in the Alfvén wing compared to the undisturbed convective electric field in Strobel *et al.* [2002] of $7 \cdot 10^{-4}$ is approximately equal to the ratio of $1 \cdot 10^{-3}$ obtained here.

4. Conclusions

This study has presented modeling results of the interaction between Callisto's ionosphere and the Jovian magnetospheric plasma environment. Since the gyroradii of pickup ions are large compared to Callisto, we use a hybrid simulation code to resolve large asymmetric structures that manifest near the moon. The interaction at three distinct orbital locations of the moon was investigated by systematically changing the angle between photoionization and plasma corotation. Because Callisto's distance to the Jovian magnetospheric current sheet varies during the course of the moon's orbit, model runs with different values of the background magnetic field were examined as well. This study investigated the contribution of the magnetosphere-ionosphere interaction in isolation, which facilitates the understanding of complex magnetic signatures observed near the moon. The results of this study suggest the following:

1. The electromagnetic field perturbations generated by the interaction between the Jovian magnetospheric plasma and Callisto's ionosphere show a high degree of robustness against changes in the orbital position or solar phase angle, in the sense that these signatures undergo only slight changes as the moon orbits Jupiter for a constant distance to the center of the Jovian current sheet. The differences that materialize as a result of the changing orbital position are minimal between each location and may be difficult to detect over fluctuations of the ambient magnetospheric field. Even though the scale height used in this study is increased by a factor of 10, the effects of changing atmospheric orientation are weak. In reality, with scale heights for the atmosphere on the order of 23 km, compared to the plasma interaction scales of $1-10 R_C$, the impact of changing atmospheric orientation would be even weaker. As a result, in studying the magnetosphere-ionosphere interaction of Callisto, the detailed structure of the atmosphere and ionosphere does not need to be resolved. This holds true as long as the closest approach of a spacecraft flyby occurs above multiple atmospheric scale heights. Considering that most Galileo flybys of Callisto occurred at altitudes much larger than an atmospheric scale height, this result is even more substantial and directly relevant for future studies that aim to identify magnetic induction signals in magnetic field data.
2. Differences in the magnetosphere-ionosphere interaction that are visible as a function of Callisto's orbital position affect mainly the pickup ion density and bulk velocity. These differences arise mainly in regions

of low pickup ion density where currents are weak and are therefore unable to noticeably influence the magnetic field near the moon.

3. When embedded in the weak magnetic field of Jupiter's magnetodisk current sheet, the strength of the magnetic signal generated by the interaction between the magnetospheric plasma and Callisto's ionosphere locally exceeds the ambient magnetospheric field magnitude by a factor of more than twice the background field and is therefore much stronger than any magnetic signal generated by induction in a putative subsurface ocean. Especially at the ramside of Callisto, the magnetic field perturbations driven by the magnetosphere-ionosphere interaction can easily obscure any fields generated by induction effects. As a result, flybys through the ramside pileup region when the moon is embedded in the Jovian current sheet would only be useful in further understanding the magnetosphere-ionosphere interaction in isolation. On the other hand, when embedded in one of the lobes of the Jovian magnetodisk, induction signals can dominate the magnetic field perturbations near the moon. However, the signal generated by the magnetosphere-ionosphere interaction is still of appreciable magnitude (with a relative strength of about 0.2 times the background field) and may not be neglected when studying the coupled interaction scenario that includes magnetic signatures driven by induction as well as the plasma interaction.
4. To explain Galileo plasma measurements of enhanced electron density during the C3 and C10 flybys through Callisto's wake, inclusion of the moon's atmosphere and ionosphere is necessary. Previous studies that lack an atmosphere in their model are unable to match the density increases by 2 orders of magnitude, as the transport of magnetospheric particles into the wake only accounts for an approximate doubling of the background density value at most.
5. Along the direction of the magnetospheric background magnetic field, Callisto's pickup tail is flat and symmetric, confined to $1-2 R_C$. However, in planes perpendicular to the background magnetic field, the plasma interaction with Callisto's ionosphere exhibits nonnegligible asymmetries. Gyration of ionospheric particles drives the pickup tail into the hemisphere where the undisturbed convective electric field points away from the moon. The pickup ions move along cycloidal arcs that are comparable to or even clearly exceed the size of Callisto's radius. A simulation model that treats these pickup ions kinetically is therefore required to resolve the asymmetries of Callisto's interaction.

The present study provides the basis for understanding the complete, entangled interaction scenario that occurs at Callisto. Our future studies of the moon's interaction with the Jovian magnetospheric environment will include the coupling of the magnetosphere-ionosphere interaction with magnetic fields generated via induction in a subsurface ocean.

Appendix A: Comparison to Galileo Flyby Data

Magnetic field flyby data from C3 and C9 are compared to the hybrid model A.I.K.E.F., with the model including an induced dipole at Callisto. *Zimmer et al. [2000]* have suggested that the ionospheric interaction was minimized during the C3 and C9 flybys, and therefore, the results presented in this section consider only the plasma-dipole interaction. These simulations are used for the purpose of validating the hybrid model with results presented previously in the literature.

For both flybys, upstream parameters as presented in Table 2 are used with the exception of the background magnetic field vector (and thus also any quantities affected by the magnitude of $|\mathbf{B}_0|$). For the C3 flyby, we set $\mathbf{B}_0 = (B_{x,0} \hat{\mathbf{x}} + B_{y,0} \hat{\mathbf{y}} + B_{z,0} \hat{\mathbf{z}}) = (-2.4 \hat{\mathbf{x}} - 31.7 \hat{\mathbf{y}} - 10.8 \hat{\mathbf{z}})$ nT, while for the C9 flyby, we set $\mathbf{B}_0 = (3.3 \hat{\mathbf{x}} + 33.9 \hat{\mathbf{y}} - 9.4 \hat{\mathbf{z}})$ nT. With these background magnetic field values, the induced magnetic moment of Callisto, \mathbf{M}_{ind} , can be calculated using

$$\mathbf{M}_{\text{ind}} = -\frac{2\pi R_C}{\mu_0} A (B_{x,0} \hat{\mathbf{x}} + B_{y,0} \hat{\mathbf{y}}) , \quad (\text{A1})$$

where we set the amplitude A —which is determined by parameters of Callisto's subsurface ocean—to 0.85 (see *Zimmer et al. [2000]*, *Saur et al. [2010]*, or *Lindkvist et al. [2015]*, for further discussion).

Magnetic field data from the Galileo magnetometer are plotted in black in Figure A1 for the (a) C3 and (b) C9 flybys of Callisto. The pure dipolar field corresponding to \mathbf{M}_{ind} in equation (A1) is displayed in red, and plotted in blue is the result of running the A.I.K.E.F. hybrid simulation with this induced dipolar magnetic field included. The overall structure of the pure dipolar field generated by \mathbf{M}_{ind} for each flyby agrees well with measured magnetic field data, which is consistent with the findings of *Zimmer et al. [2000]*. However, especially in B_y

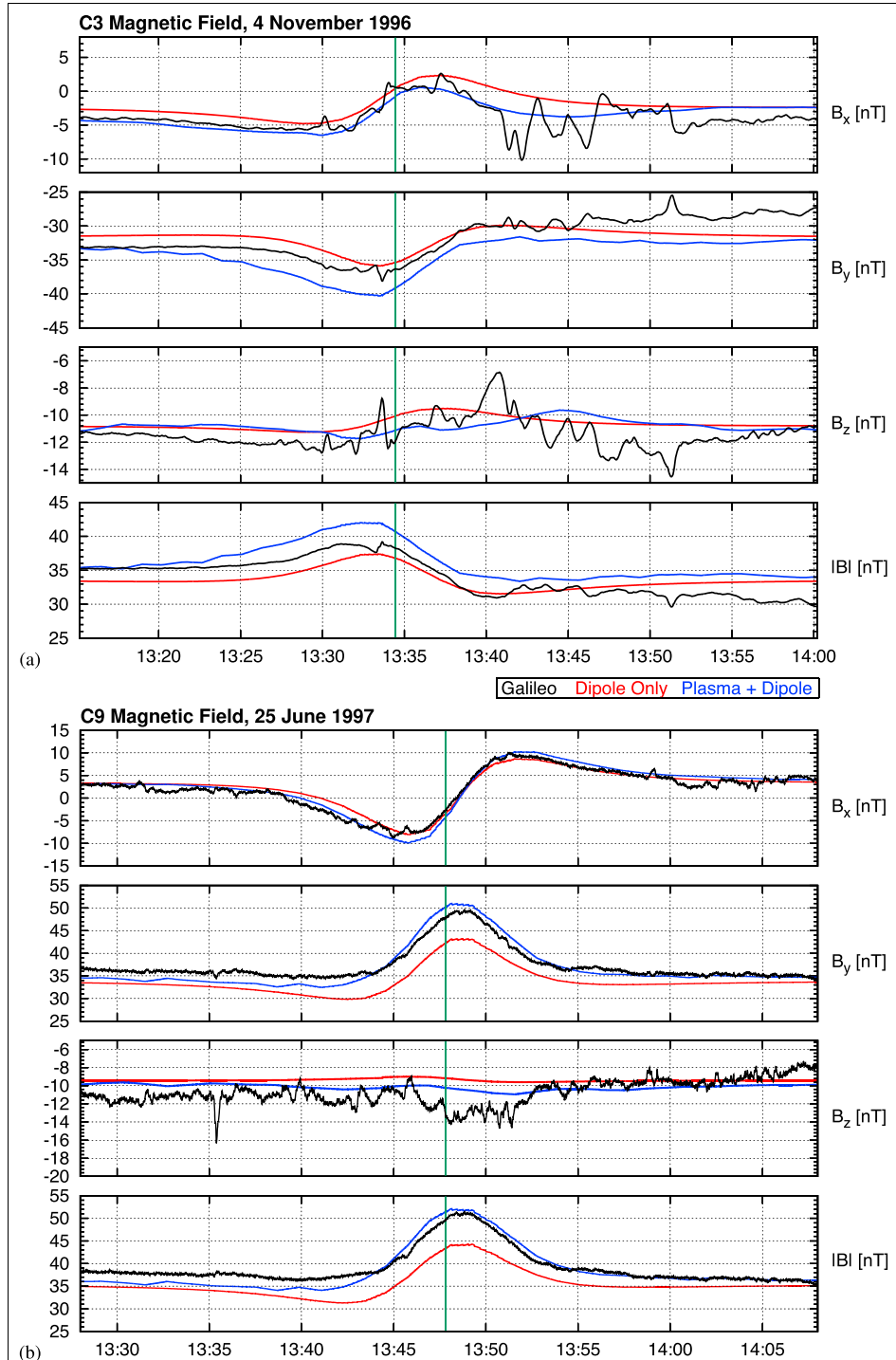


Figure A1. Magnetic field signatures from the (a) C3 and (b) C9 flybys. In black is the measured Galileo magnetic field, in red is a pure dipolar magnetic field, and in blue is the result of the A.I.K.E.F. hybrid simulation code run with the induced dipolar field. The time of closest approach to Callisto is marked by the vertical green line.

and $|\mathbf{B}|$, the magnetic field generated by a purely dipolar field is slightly offset in magnitude from the actual magnetic field measured by Galileo. By simulating the moon's plasma interaction with an induced dipole in the hybrid model (blue lines), the magnetic field along each of the flyby trajectories is closer to the observed field value, as the plasma interaction compresses the dipole magnetic field lines generated by induction in a subsurface ocean. These results are consistent with the findings presented in *Khurana et al.* [1998], *Kivelson et al.* [1999], *Zimmer et al.* [2000], and *Lindkvist et al.* [2015] and show that A.I.K.E.F. is able to reproduce Galileo data at least as accurately as previously published studies.

We would again like to emphasize that running the hybrid simulation with inclusion of both, Callisto's atmosphere and an induced magnetic moment, would be a completely new paper on its own and is beyond the scope of the present study.

Acknowledgments

The work of Lucas Liuzzo and Sven Simon was supported by NASA through the *Solar System Workings 2014* program grant NNX15AL52G. The source code used to generate the simulation results and the data used to render the figures are available from the corresponding author upon request, and Galileo flyby data are available at the Planetary Data System. The authors would like to thank the reviewers for their valuable feedback on the manuscript.

References

- Bagdonat, T. (2005), Hybrid simulation of weak comets, PhD thesis, Technische Universität zu Braunschweig. [Available at [http://digisrv-1.biblio/etc.tu-bs.de:8080/docportal/receive/DocPortal_document_00000011;jsessionid=93338E95769867F5F6372FC9D408596B?lang=en.\]](http://digisrv-1.biblio/etc.tu-bs.de:8080/docportal/receive/DocPortal_document_00000011;jsessionid=93338E95769867F5F6372FC9D408596B?lang=en.)
- Bagenal, F., and P. A. Delamere (2011), Flow of mass and energy in the magnetospheres of Jupiter and Saturn, *J. Geophys. Res.*, 116, A05209, doi:10.1029/2010JA016294.
- Belcher, J. W. (1983), The low-energy plasma in the Jovian magnetosphere, *Phys. Jovian Magnetos.*, 1, 68–105.
- Benna, M., et al. (2010), Modeling of the magnetosphere of Mercury at the time of the first MESSENGER flyby, *Icarus*, 209(1), 3–10.
- Bößwetter, A., T. Bagdonat, U. Motschmann, and K. Sauer (2004), Plasma boundaries at Mars: A 3-D simulation study, *Ann. Geophys.*, 22(12), 4363–4379, doi:10.5194/angeo-22-4363-2004.
- Carlson, R. W. (1999), A tenuous carbon dioxide atmosphere on Jupiter's moon Callisto, *Science*, 283(5403), 820–821, doi:10.1126/science.283.5403.820.
- Chamberlin, P. C., T. N. Woods, and F. G. Eparvier (2007), Flare Irradiance Spectral Model (FISM): Daily component algorithms and results, *Space Weather*, 5, S07005, doi:10.1029/2007SW000316.
- Coates, A. J., et al. (2012), Cassini in Titan's tail: CAPS observations of plasma escape, *J. Geophys. Res.*, 117, A05324, doi:10.1029/2012JA017595.
- Cunningham, N. J., J. R. Spencer, P. D. Feldman, D. F. Strobel, K. France, and S. N. Osterman (2015), Detection of Callisto's oxygen atmosphere with the Hubble Space Telescope, *Icarus*, 254, 178–189.
- Dougherty, M. K., K. K. Khurana, F. M. Neubauer, C. T. Russell, J. Saur, J. S. Leisner, and M. E. Burton (2006), Identification of a dynamic atmosphere at Enceladus with the Cassini magnetometer, *Science*, 311(5766), 1406–1409, doi:10.1126/science.1120985.
- Feyerabend, M., S. Simon, U. Motschmann, and L. Liuzzo (2015), Filamented ion tail structures at Titan: A hybrid simulation study, *Planet. Space Sci.*, 117, 362–376, doi:10.1016/j.pss.2015.07.008.
- Gurnett, D. A., W. S. Kurth, R. R. Shaw, A. Roux, R. Gendrin, C. F. Kennel, F. L. Scarf, and S. D. Shawhan (1992), The Galileo plasma wave investigation, *Space Sci. Rev.*, 60, 341–355.
- Gurnett, D. A., W. S. Kurth, A. Roux, and S. J. Bolton (1997), Absence of a magnetic-field signature in plasma-wave observations at Callisto, *Nature*, 387(6630), 261–262, doi:10.1038/387261a0.
- Gurnett, D. A., A. M. Persoon, W. S. Kurth, A. Roux, and S. J. Bolton (2000), Plasma densities in the vicinity of Callisto from Galileo plasma wave observations, *Geophys. Res. Lett.*, 27(13), 1867–1870, doi:10.1029/2000GL003751.
- Joy, S. P., M. G. Kivelson, R. J. Walker, K. K. Khurana, C. T. Russell, and T. Ogino (2002), Probabilistic models of the Jovian magnetopause and bow shock locations, *J. Geophys. Res.*, 107, 1309, doi:10.1029/2001JA009146.
- Khurana, K. K. (1997), Euler potential models of Jupiter's magnetospheric field, *J. Geophys. Res.*, 102, 11,295–11,306, doi:10.1029/97JA00563.
- Khurana, K. K., and M. G. Kivelson (1993), Inference of the angular velocity of plasma in the Jovian magnetosphere from the sweepback of magnetic field, *J. Geophys. Res.*, 98, 67–79, doi:10.1029/92JA01890.
- Khurana, K. K., M. G. Kivelson, C. T. Russell, R. J. Walker, and D. J. Southwood (1997), Absence of an internal magnetic field at Callisto, *Nature*, 387(6630), 262–264, doi:10.1038/387262a0.
- Khurana, K. K., M. G. Kivelson, D. J. Stevenson, G. Schubert, C. T. Russell, R. J. Walker, and C. Polanskey (1998), Induced magnetic fields as evidence for subsurface oceans in Europa and Callisto, *Nature*, 395(6704), 777–780, doi:10.1038/27394.
- Kivelson, M. G., K. K. Khurana, D. J. Stevenson, L. Bennett, S. Joy, C. T. Russell, R. J. Walker, C. Zimmer, and C. Polanskey (1999), Europa and Callisto: Induced or intrinsic fields in a periodically varying plasma environment, *J. Geophys. Res.*, 104(A3), 4609–4626, doi:10.1029/1998JA900095.
- Kivelson, M. G., F. Bagenal, W. S. Kurth, F. M. Neubauer, C. Paranicas, and J. Saur (2004), Magnetospheric interactions with satellites, in *Jupiter: The Planet, Satellites and Magnetosphere*, edited by M. G. Kivelson et al., pp. 513–536, Cambridge Univ. Press, Cambridge, U. K.
- Kliore, A. J., A. Anabtawi, R. G. Herrera, S. W. Asmar, A. F. Nagy, D. P. Hinson, and F. M. Flasar (2002), Ionosphere of Callisto from Galileo radio occultation observations, *J. Geophys. Res.*, 107, 1407, doi:10.1029/2002JA009365.
- Kriegel, H. (2014), The plasma environment of Saturn's moons Enceladus and Rhea: Modeling of Cassini magnetic field data, PhD thesis, Technische Universität zu Braunschweig. [Available at [http://digisrv-1.biblio/etc.tu-bs.de:8080/docportal/receive/DocPortal_document_00056094?lang=en.\]](http://digisrv-1.biblio/etc.tu-bs.de:8080/docportal/receive/DocPortal_document_00056094?lang=en.)
- Kriegel, H., S. Simon, J. Müller, U. Motschmann, J. Saur, K. Glassmeier, and M. K. Dougherty (2009), The plasma interaction of Enceladus: 3D hybrid simulations and comparison with Cassini MAG data, *Planet. Space Sci.*, 57(14–15), 2113–2122, doi:10.1016/j.pss.2009.09.025.
- Kriegel, H., S. Simon, U. Motschmann, J. Saur, F. M. Neubauer, A. M. Persoon, M. K. Dougherty, and D. A. Gurnett (2011), Influence of negatively charged plume grains on the structure of Enceladus' Alfvén wings: Hybrid simulations versus Cassini MAG data, *J. Geophys. Res.*, 116, A10223, doi:10.1029/2011JA016842.
- Kriegel, H., S. Simon, P. Meier, U. Motschmann, J. Saur, A. Wennmacher, D. F. Strobel, and M. K. Dougherty (2014), Ion densities and magnetic signatures of dust pick-up at Enceladus, *J. Geophys. Res. Space Physics*, 119, 2740–2774, doi:10.1002/2013JA019440.
- Ledvina, S. A., S. H. Brecht, and T. E. Cravens (2012), The orientation of Titan's dayside ionosphere and its effects on Titan's plasma interaction, *Earth Planets Space*, 64, 207–230.

- Liang, M.-C., B. F. Lane, R. T. Pappalardo, M. Allen, and Y. L. Yung (2005), Atmosphere of Callisto, *J. Geophys. Res.*, **110**, E02003, doi:10.1029/2004JE002322.
- Lindkvist, J., M. Holmström, K. Khurana, S. Fatemi, and S. Barabash (2015), Callisto plasma interactions: Hybrid modeling including induction by a subsurface ocean, *J. Geophys. Res. Space Physics*, **120**, 4877–4889, doi:10.1002/2015JA021212.
- Müller, J., S. Simon, U. Motschmann, K. H. Glassmeier, J. Saur, J. Schuele, and G. J. Pringle (2010), Magnetic field fossilization and tail reconfiguration in Titan's plasma environment during a magnetopause passage: 3D adaptive hybrid code simulations, *Planet. Space Sci.*, **58**(12), 1526–1546, doi:10.1016/j.pss.2010.07.018.
- Müller, J., S. Simon, U. Motschmann, J. Schüle, K. Glassmeier, and G. J. Pringle (2011), A.I.K.E.F.: Adaptive hybrid model for space plasma simulations, *Comput. Phys. Commun.*, **182**(4), 946–966, doi:10.1016/j.cpc.2010.12.033.
- Neubauer, F. M. (1980), Nonlinear standing Alfvén wave current system at Io: Theory, *J. Geophys. Res.*, **85**, 1171–1178, doi:10.1029/JA085iA03p01171.
- Neubauer, F. M. (1998), The sub-Alfvénic interaction of the Galilean satellites with the Jovian magnetosphere, *J. Geophys. Res.*, **103**, 19,843–19,866, doi:10.1029/97JE03370.
- Neubauer, F. M. (1999), Alfvén wings and electromagnetic induction in the interiors: Europa and Callisto, *J. Geophys. Res.*, **104**, 28,671–28,684, doi:10.1029/1999JA900217.
- Neubauer, F. M., D. A. Gurnett, J. D. Scudder, and R. E. Harte (1984), Titan's magnetospheric interaction, in *Saturn*, edited by T. Gehrels and M. S. Matthews, pp. 760–787, Univ. of Arizona Press, Tucson, Ariz.
- Neubauer, F. M., et al. (2006), Titan's near magnetotail from magnetic field and plasma observations and modelling: Cassini flybys TA, TB and T3, *J. Geophys. Res.*, **111**, A10220, doi:10.1029/2006JA011676.
- Richards, P. C., J. A. Fennelly, and D. G. Torr (1994), EUVAC: A solar EUV flux model for aeronomics calculations, *J. Geophys. Res.*, **99**, 8981–8992.
- Richards, P. G., T. N. Woods, and W. K. Peterson (2006), HEUVAC: A new high resolution solar EUV proxy model, *Adv. Space Res.*, **37**(2), 315–322.
- Roussos, E., J. Mueller, S. Simon, A. Boesswetter, U. Motschmann, N. Krupp, M. Fraenz, J. Woch, K. K. Khurana, and M. K. Dougherty (2008), Plasma and fields in the wake of Rhea: 3-D hybrid simulation and comparison with Cassini data, *Ann. Geophys.*, **26**(3), 619–637.
- Saur, J., F. M. Neubauer, D. F. Strobel, and M. E. Summers (1999), Three-dimensional plasma simulation of Io's interaction with the Io plasma torus: Asymmetric plasma flow, *J. Geophys. Res.*, **104**(A11), 25,105–25,126, doi:10.1029/1999JA900304.
- Saur, J., F. M. Neubauer, and K.-H. Glassmeier (2010), Induced magnetic fields in solar system bodies, *Space Sci. Rev.*, **152**(1–4), 391–421.
- Schunk, R. W., and A. F. Nagy (2009), *Ionospheres: Physics, Plasma Physics, and Chemistry*, 2nd ed., Cambridge Univ. Press, Cambridge, U. K.
- Seufert, M. (2012), Callisto: Induction signals, atmosphere and plasma interaction, PhD thesis, Universität zu Köln. [Available online at <http://kups.ub.uni-koeln.de/4903>.]
- Seufert, M., J. Saur, and F. M. Neubauer (2011), Multi-frequency electromagnetic sounding of the Galilean moons, *Icarus*, **214**(2), 477–494, doi:10.1016/j.icarus.2011.03.017.
- Simon, S., and U. Motschmann (2009), Titan's induced magnetosphere under non-ideal upstream conditions: 3D multi-species hybrid simulations, *Planet. Space Sci.*, **57**(14–15), 2001–2015, doi:10.1016/j.pss.2009.08.010.
- Simon, S., A. Boesswetter, T. Bagdonat, U. Motschmann, and K.-H. Glassmeier (2006), Plasma environment of Titan: A 3-D hybrid simulation study, *Ann. Geophys.*, **24**(3), 1113–1135.
- Simon, S., A. Boesswetter, T. Bagdonat, U. Motschmann, and J. Schuele (2007), Three-dimensional multispecies hybrid simulation of Titan's highly variable plasma environment, *Ann. Geophys.*, **25**(1), 117–144.
- Simon, S., U. Motschmann, and K.-H. Glassmeier (2008), Influence of non-stationary electromagnetic field conditions on ion pick-up at Titan: 3-D multispecies hybrid simulations, *Ann. Geophys.*, **26**(3), 599–617.
- Simon, S., J. Saur, F. Neubauer, U. Motschmann, and M. Dougherty (2009), Plasma wake of Tethys: hybrid simulations versus Cassini MAG data, *Geophys. Res. Lett.*, **36**(4), L04108, doi:10.1029/2008GL036943.
- Simon, S., H. Kriegel, J. Saur, A. Wennmacher, F. M. Neubauer, E. Roussos, U. Motschmann, and M. K. Dougherty (2012), Analysis of Cassini magnetic field observations over the poles of Rhea, *J. Geophys. Res.*, **117**, A07211, doi:10.1029/2012JA017747.
- Strobel, D. F., J. Saur, P. D. Feldman, and M. A. McGrath (2002), Hubble Space Telescope space telescope imaging spectrograph search for an atmosphere on Callisto: A Jovian unipolar inductor, *Astrophys. J.*, **581**(1), L51–L54, doi:10.1086/345803.
- Vorburger, A., P. Wurz, H. Lammer, S. Barabash, and O. Mousis (2015), Monte Carlo simulation of Callisto's exosphere, *Icarus*, **262**, 14–29.
- Zimmer, C., K. K. Khurana, and M. G. Kivelson (2000), Subsurface oceans on Europa and Callisto: Constraints from Galileo magnetometer observations, *Icarus*, **147**(2), 329–347, doi:10.1006/icar.2000.6456.